Chapter 4

Chapter 4

Strategically developed plasmonic-activated heterojunction system for high-efficiency visible-light-driven photocatalysis

The tunability of light absorption across a broad spectral range, along with enhanced generation of electron-hole pairs, can be effectively achieved through the sensitization of host semiconductors with plasmonic metal nanostructures. This chapter focuses on enhancing the photocatalytic performance of a heterojunction-based TiO_2 photocatalyst through plasmonic sensitization using Ag nanoparticles as a co-catalyst. Ag metal nanoparticles support surface plasmon resonance (SPR) phenomena that can boost the electron population in the conduction band of the host semiconductor, thereby enhancing photocatalytic efficiency. Metallic Ag nanoparticles can also form a Schottky junction with TiO_2, which promotes a unidirectional charge transfer from Ag to TiO_2, preventing back migration. With suitable tuning of the size and shape of Ag particles, the wavelength of plasmonic resonance can be adjusted within the visible light range. This, in turn, facilitates the development of an enhanced plasmon-assisted heterojunction photocatalyst with superior activity under visible light irradiation. A bulbous branched plasmonic Ag nanostructure assisted Cu_2O-CuO/TiO_2 heterojunction photocatalyst was thus prepared using a facile sol-gel technique, and its MB degradation efficiency was explored. The physicochemical, morphostructural, and spectroscopic characteristics were studied using XRD, UV-vis-DRS, SEM, TEM, Raman, ESR, and XPS. The current study demonstrates an integrated plasmonic-heterojunction photocatalytic system that offers a promising avenue for enhancing photocatalytic performance in dye-contaminated water treatment.

4.1. Introduction

Plasmonic photocatalysts have garnered considerable attention due to the unique phenomenon of plasmonic resonance, which offers light absorption tunability throughout a wide range of spectral regions [1]. Several studies have reported on the enhancement of the photocatalytic activity using different shapes and sizes of plasmonic metals, with increasing visible light response [2-5]. This enhancement arises from the different localized surface plasmon resonance (LSPR) effects involved in the plasmonic photocatalysis, as discussed in Chapter 1. Among plasmonic metals, silver nanoparticles (Ag NPs) are especially notable for their high-quality factor over the near UV-Vis-IR

spectrum, as well as for their superior electrical and thermal conductivity [6]. Ag nanostructures can be readily synthesized to absorb and scatter light in the visible and near-UV regions, resulting in the generation of strong local electric fields around the nanoparticles [7]. This induced LSPR can significantly reduce photoexcited charge carrier recombination and facilitate electron injection from plasmonic metal to host semiconductor [8]. Additionally, in metal-semiconductor composites, the average photon path length increases as a result of the light absorption and re-emission in plasmonic metals, resulting in a higher activation rate of incident photons. Therefore, the incorporation of suitably engineered Ag nanoparticles into a heterojunction semiconductor photocatalyst is highly likely to result in a significant enhancement of photocatalytic performance. Further, in comparison to single-component systems, multicomponent heterojunction systems comprising multiple activated components have been demonstrated to enable efficient spatial separation of photo-induced electron-hole pairs via sequential charge transfer at the interfaces, resulting in enhanced photocatalytic performance [9]. The formation of multiple p-n junctions and the LSPR effect of Ag nanoparticles in M@Cu_xO/ZnO (M = Au, Ag) demonstrated improved visible-light-driven catalytic activity, which is ascribed to the synergistic effect of the wider spectral band, efficient transfer of photogenerated charge carriers, and strong LSPR impact [10]. Thus, herein, we have initially synthesized bulbous structured Ag nanoparticles using a facile method and later sensitized them on Cu_2O/TiO_2 heterojunction photocatalyst and finally obtained a plasmonic-heterojunction hybrid material (Ag@Cu_2O-CuO/TiO_2) via a post thermal treatment. The Cu_2O-CuO/TiO_2 ternary junction enhanced the charge carrier separation through the interface between the semiconductors. The mismatch in band edge positions between Cu_2O, CuO, and TiO_2 produces a built-in field near the junctions that plays a vital role in boosting the photocatalytic performance. Additionally, the bulbous Ag nanoparticles exhibit broad absorption across the visible range, which further enhances the catalyst's performance in visible light. Methylene blue (MB) was used as a test pollutant for photocatalytic degradation. The plasmonic charge carrier injection into the photocatalyst and the ease of the charge transfer between the interface were demonstrated via a ternary interfacial junction.

4.2. Experimental details

4.2.1. Materials and methods

The reagents that were used for preparing the photocatalysts are: Titanium isopropoxide [$Ti(OCH(CH_3)_2)_4$] was purchased from Alfa Aesar. Silver nitrate [$AgNO_3$], 2-propanol [$(CH_3)_2CHOH$], Ammonia solution [NH_3], Ascorbic acid [$C_6H_8O_6$], and nitric acid [HNO_3] were supplied by Merck, India. Sodium hydroxide pellets [NaOH] and copper sulfate pentahydrate [$CuSO_4.5H_2O$] were obtained from Avantor Performance Materials India Limited. Ammonium oxalate [$(NH_4)_2C_2O_4$] was purchased from Rankem, India, and p-Benzoquinone [$C_6H_4O_2$] from Sigma-Aldrich, and L-histidine [$C_6H_9N_3O_2$] was obtained from Loba, Chemie.

In the synthesis of pure TiO_2, a mixture of $Ti(OCH(CH_3)_2)_4$ and $(CH_3)_2CHOH$ at a particular 1:10 volume ratio was obtained and stirred rapidly. Half an hour later, 200 μL of H_2O was added dropwise under stirring conditions. Again, after 30 minutes, 1 ml of 1M HNO_3 was added to the mixture. This mixture solution was continuously kept under stirring conditions for the next 24 hours. A semi-gel precipitation was obtained after aging for a few hours. The product was then dried at 80-100 ^oC, followed by pulverization into a fine powder, and then finally calcined at 600 ^oC for two hours.

To obtain the CuO co-catalyst, a simple wet-chemical procedure was adopted that required a moderately low temperature (~80 ^oC) condition. First, a 100 mL solution of 0.0216 M copper sulfate pentahydrate ($CuSO_4.5H_2O$) was prepared. Afterward, 500 μL of 14.7 M ammonium solution was added under constant stirring conditions. Next, 25 mL NaOH (0.1 M) solution was mixed with the above suspension followed by 10 mL ascorbic acid (0.1 M) addition and kept at ~80 ^oC for 50 minutes under constant stirring. After obtaining a red-brown precipitate, it was washed several times and calcined for two hours at 600 ºC.

In a typical synthesis of bulbous branched Ag nanostructure, 10 ml L-ascorbic acid (4.6 mM) was blended with 10 ml silver nitrate ($AgNO_3$), and the resultant mixture was centrifuged to obtain the Ag product.

In order to synthesize CuO/TiO_2, 2 mL titanium isopropoxide was initially added to 20 mL isopropanol. After 30 minutes of vigorous stirring, 0.1 g of previously prepared CuO dispersed uniformly in 50 mL isopropanol was added. Then, after 50 minutes, 1 mL of concentrated HNO_3 solution was mixed with the solution. The

suspension was stirred for 24 hours and kept in the ambient condition for another 24 hours. The obtained sample was ground into a fine powder and calcined at 600˚C for two hours.

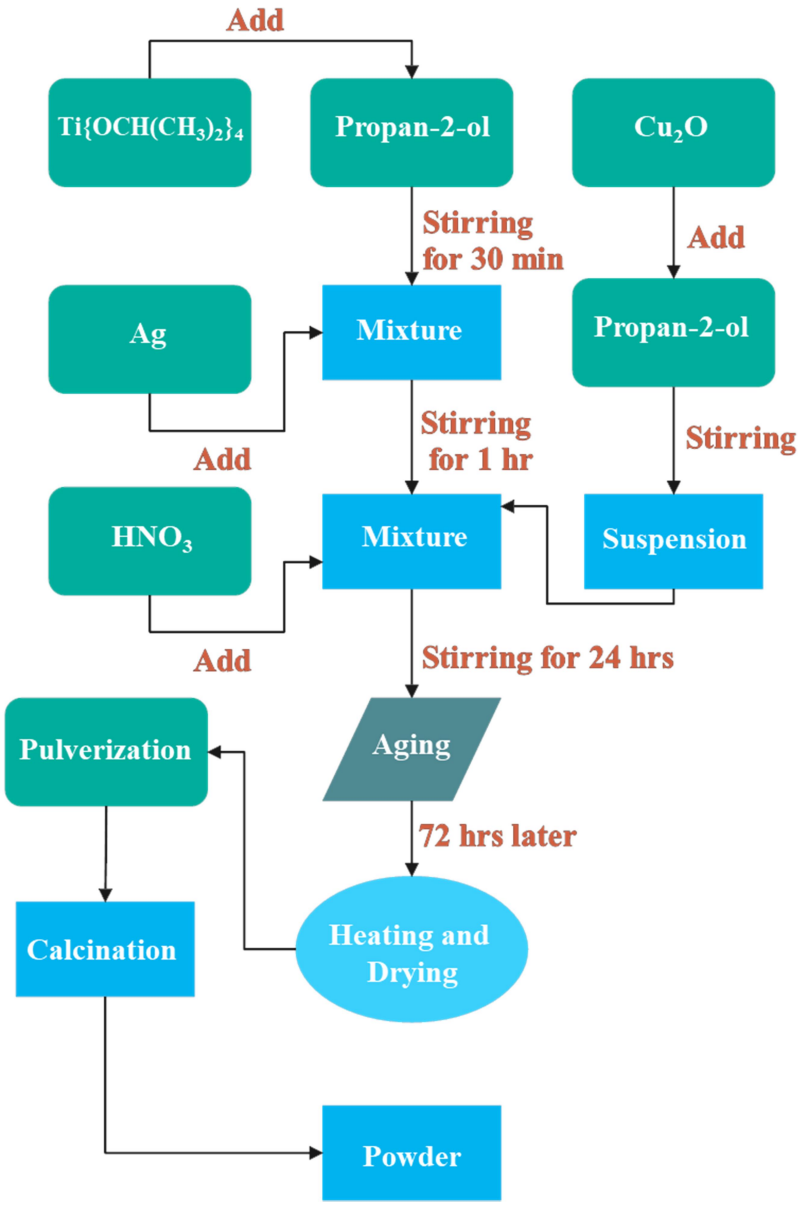

Figure 4.1. Block diagram illustrating the synthesis of Ag@Cu_2O-CuO/TiO_2.

In the Ag@Cu_2O-CuO/TiO_2 photocatalyst synthesis, Ti(IV)-isopropoxide and isopropanol were mixed by stirring it constantly and vigorously. After 30 minutes, 0.0045 g of well-dispersed Ag was added to the solution. Subsequently, 0.20 g of Cu_2O was uniformly dispersed in 50 mL isopropanol, and 1 mL of concentrated HNO_3 was added to the mixture. The mixture was stirred for 24 hours and then left to age for 72

hours. Finally, the supernatant was discarded, and the obtained product was calcined at 600˚C for two hours. A block diagram representation of the synthesis procedure is provided in Figure 4.1.

4.2.2. Characterization

The photocatalysts were characterized using the following analysis techniques: XRD, UV-visible DRS, Raman, ESR, photoluminescence, XPS, SEM, and TEM. The details of the instrument for the technique have been provided in Chapter 2. The photocatalytic performance of the photocatalysts was evaluated against MB and Phenol dye degradation, following the procedures as described in Chapter 2.

4.3. Results and discussion

4.3.1. XRD and UV-vis-DRS analysis

XRD patterns of TiO_2, CuO, CuO/TiO_2 and $Ag@Cu_2O$-CuO/TiO_2 are shown in Figure 4.2.

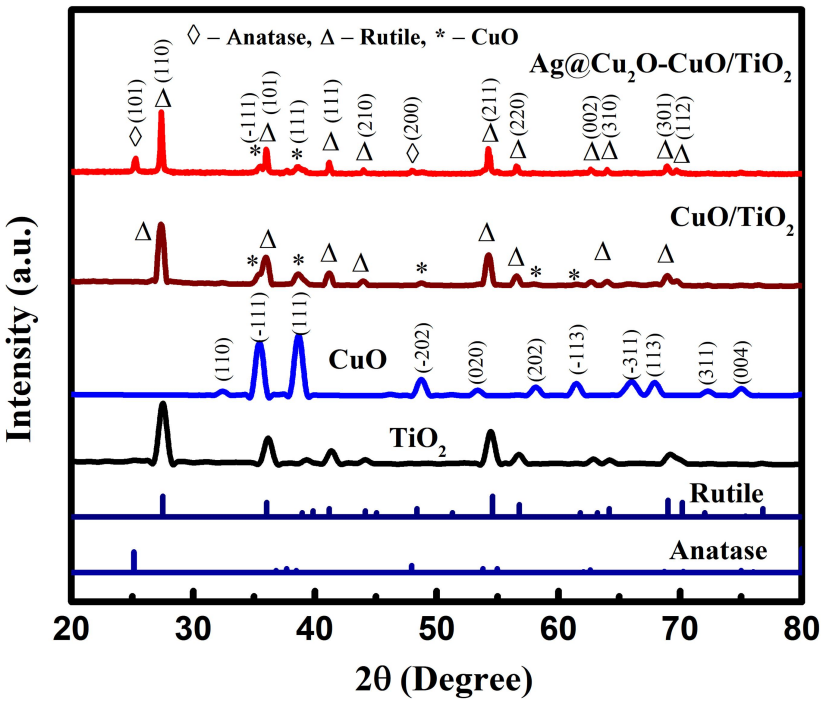

Figure 4.2. XRD patterns of TiO_2, CuO, CuO/TiO_2, and $Ag@Cu_2O$-CuO/TiO_2.

The diffraction spectra of pristine TiO_2, CuO/TiO_2, and $Ag@Cu_2O$-CuO/TiO_2 at 2θ = 27.4°, 36.1°, 41.3°, 44.1°, 54.2 °, 56.7 °, 64.1°, and 69.1° corresponds to the rutile phase (PDF no: 894920). These peaks represent the planes (110), (101), (111), (210), (211),

(220), (310), and (301), respectively. No peaks corresponding to the anatase phase were observed in TiO_2 and CuO/TiO_2. However, the observed peaks at $2\theta = 25.3^o$, 48.1^o, and 62.7^o in $Ag@Cu_2O\text{-}CuO/TiO_2$ are due to the anatase phase of TiO_2, which correspond to the planes (101), (200), and (204) (PDF no: 894921). The presence of the anatase phase in the $Ag@Cu_2O\text{-}CuO/TiO_2$ sample could be ascribable to the Ag incorporation which prevents the growth of the rutile phase [11].

A similar result was observed in the $Ag@TiO_2$ sample shown in Figure 4.3. The $Ag@TiO_2$ photocatalyst shows both the phases of TiO_2, i.e. anatase and rutile phase corresponding to PDF no: 89-4921 and 89-4920, respectively. Notably, the as-prepared CuO has formed only after calcination of Cu_2O (pristine) at 600 ^oC [12].

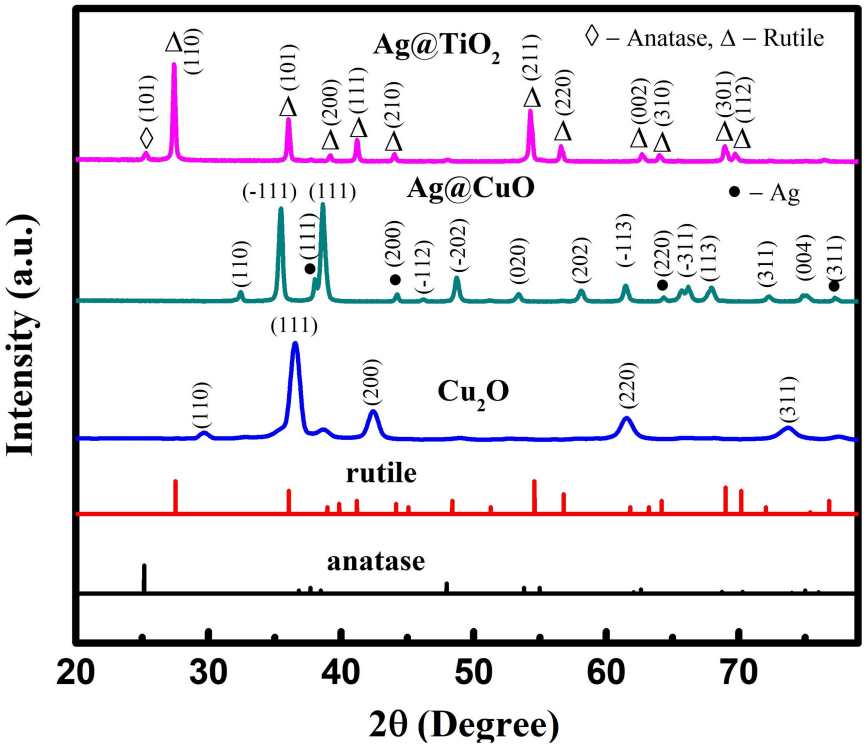

Figure 4.3. X-ray diffraction spectra of Cu_2O (as-prepared), Ag@CuO calcined at 600 ^oC and $Ag@TiO_2$ calcined at 600 ^oC.

The XRD spectra of as-prepared pristine Cu_2O are shown in Figure 4.3 along with Ag@CuO (600 ^oC) and $Ag@TiO_2$ (600 ^oC). The major XRD peaks of CuO were located at $2\theta = 35.2^o$, 38.6^o, 48.7^o, 53.4^o, 61.4^o, and 67.9^o (PDF no: 892530). The presence of CuO is confirmed by the appearance of peaks at 35.2^o and 38.6^o in CuO/TiO_2 and $Ag@Cu_2O\text{-}CuO/TiO_2$. However, the peaks related to Cu_2O and Ag were

not observed in the XRD spectrum of Ag@Cu_2O-CuO/TiO_2, which might be due to their low concentration compared to TiO_2. The crystallite size determined by the Debye-Scherrer equation (2.2), is ~11, ~12, ~17, and ~35 nm, in CuO, TiO_2, CuO/TiO_2 and Ag@Cu_2O-CuO/TiO_2, respectively.

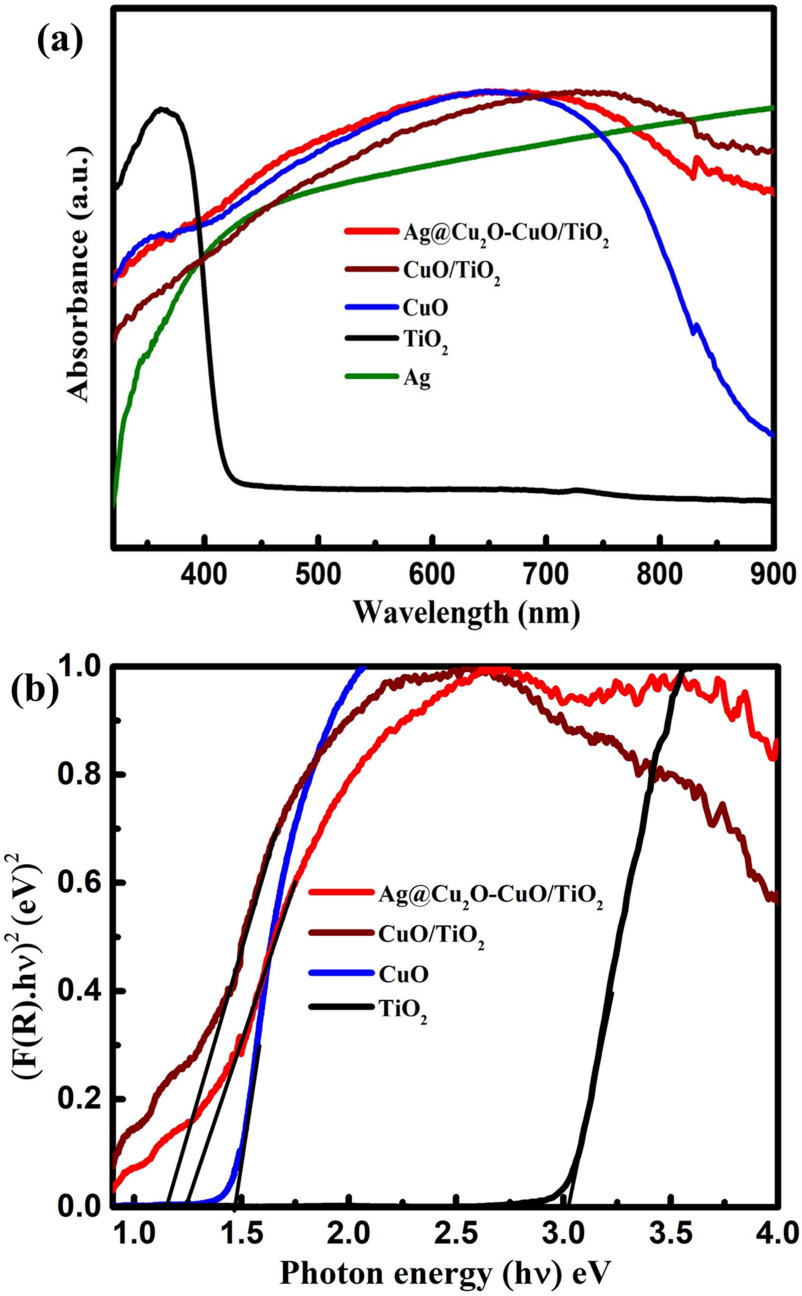

Figure 4.4. (a) UV-Vis-DRS of TiO_2, CuO, CuO/TiO_2, and Ag@Cu_2O-CuO/TiO_2 and UV-vis absorbance spectra of bulbous Ag, (b) Bandgap determination of TiO_2, CuO, CuO/TiO_2, and Ag@Cu_2O-CuO/TiO_2 using Tauc plot.

Figure 4.4 displays the absorbance spectra of TiO_2, CuO, CuO/TiO_2, and $Ag@Cu_2O$-CuO/TiO_2. Pure TiO_2 shows sharp absorption onset in the UV region at around 387 nm, while CuO/TiO_2 and $Ag@Cu_2O$-CuO/TiO_2 sample exhibits an extended absorption over the visible range of 400 to 800 nm. The absorbance spectrum of Ag is highly broad and extends into the near-infrared (NIR) region, attributable to the branched nature (illustrated in Figure 4.4) [13-14].

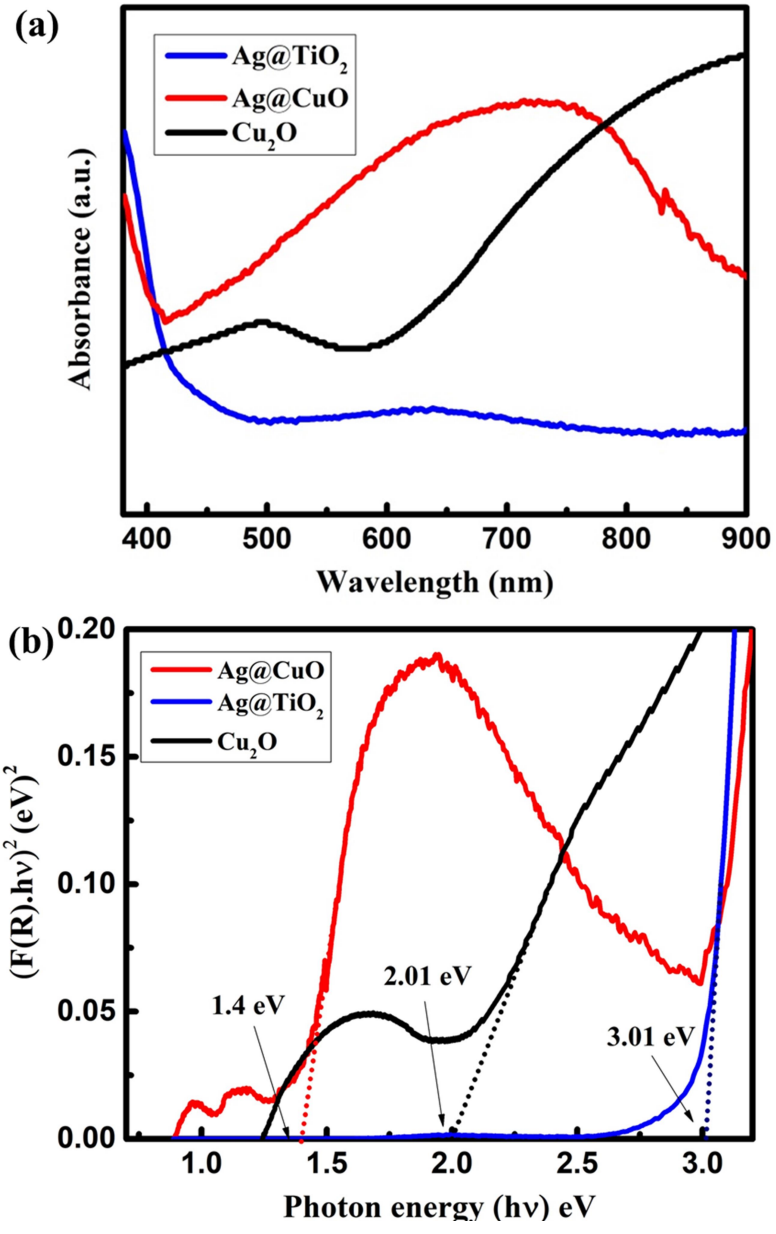

Figure 4.5. (a) UV-Vis-DRS of Cu_2O (as-prepared), Ag@CuO (600 ^oC) and $Ag@TiO_2$ (600 ^oC). (b) Bandgap determination using Tauc plot.

The Tauc plot of the Kubelka-Munk function for calculating the optical bandgap is shown in Figure 4.4(b) [15]. The obtained bandgaps of the samples are 3.02, 1.47, 1.17, and 1.24 eV for TiO_2, CuO, CuO/TiO_2, and Ag@Cu_2O-CuO/TiO_2, respectively. The absorbance spectra and the Tauc plot for determination of the bandgap of Ag@TiO_2, Ag@CuO, and Cu_2O are shown in Figure 4.5(a-b). There was no change in the bandgap of TiO_2 and CuO after Ag incorporation. The bandgap of Cu_2O (as-prepared), Ag@CuO (600 ^oC) and Ag@TiO_2 (600 ^oC) were calculated to be 2.01 eV, 1.40 eV and 3.01 eV, respectively.

4.3.2. Raman, ESR and photoluminescence analysis

The Raman spectra of TiO_2, CuO/TiO_2, and Ag@Cu_2O-CuO/TiO_2 are displayed in Figure 4.6(a). The pure TiO_2 revealed the typical stretching peaks of the rutile phase at 140, 447.1, and 607.9 cm^{-1}, which correspond to the symmetric modes B_{1g}, E_g, and A_{1g}, respectively [16-18]. Additionally, the broad and mid-intensity signal detected at 238 cm^{-1} is attributable to the two-phonon scattering of the rutile phase [18]. The peak observed at 277 (A_g) and 616 cm^{-1} (B_g) in CuO/TiO_2 and Ag@Cu_2O-CuO/TiO_2 are related to CuO [19-20]. In Ag@Cu_2O-CuO/TiO_2, the Raman signals at 144, 197, 396, and 513 cm^{-1} with symmetries of E_g, E_g, B_{1g}, and (A_{1g} + B_{1g}) represent the anatase phase, whereas the signals at 143, 443, and 608 cm^{-1} with symmetries of B_{1g}, E_g and A_{1g} denote the rutile phase [21]. Furthermore, the Raman spectrum of Ag@Cu_2O-CuO/TiO_2 reveals the presence of Cu_2O at 410 (multi-phonon scattering) and 515 cm^{-1} (T_{2g}), which accords with the XPS results [20, 22, 23]. The presence of the anatase phase in the Ag@TiO_2 counterpart was also observed as shown in Figure 4.6(a).

The electron spin resonance (ESR) study was performed to understand the presence of oxygen vacancy or Ti^{3+} in the photocatalyst. ESR spectrum of TiO_2, CuO/TiO_2, and Ag@Cu_2O-CuO/TiO_2 are displayed in Figure 4.6(b). The g-value was obtained using the relation $g = {h\nu}/{\beta H_o}$, where h is the plank constant, ν is the frequency, β is the Bohr magnetron, and H_o is the resonance magnetic field [24]. The ESR resonance peak at g = 1.98 in pure TiO_2 corresponds to the Ti^{3+} species [25]. The observed ESR signals of CuO/TiO_2 and Ag@Cu_2O-CuO/TiO_2, at g = 2.13, are attributable to Cu^{2+} [26, 27]. The ESR peak intensity at g = 2.13 is decreased

considerably after Ag incorporation in $Ag@Cu_2O$-CuO/TiO_2, indicating the formation of Cu_2O [26].

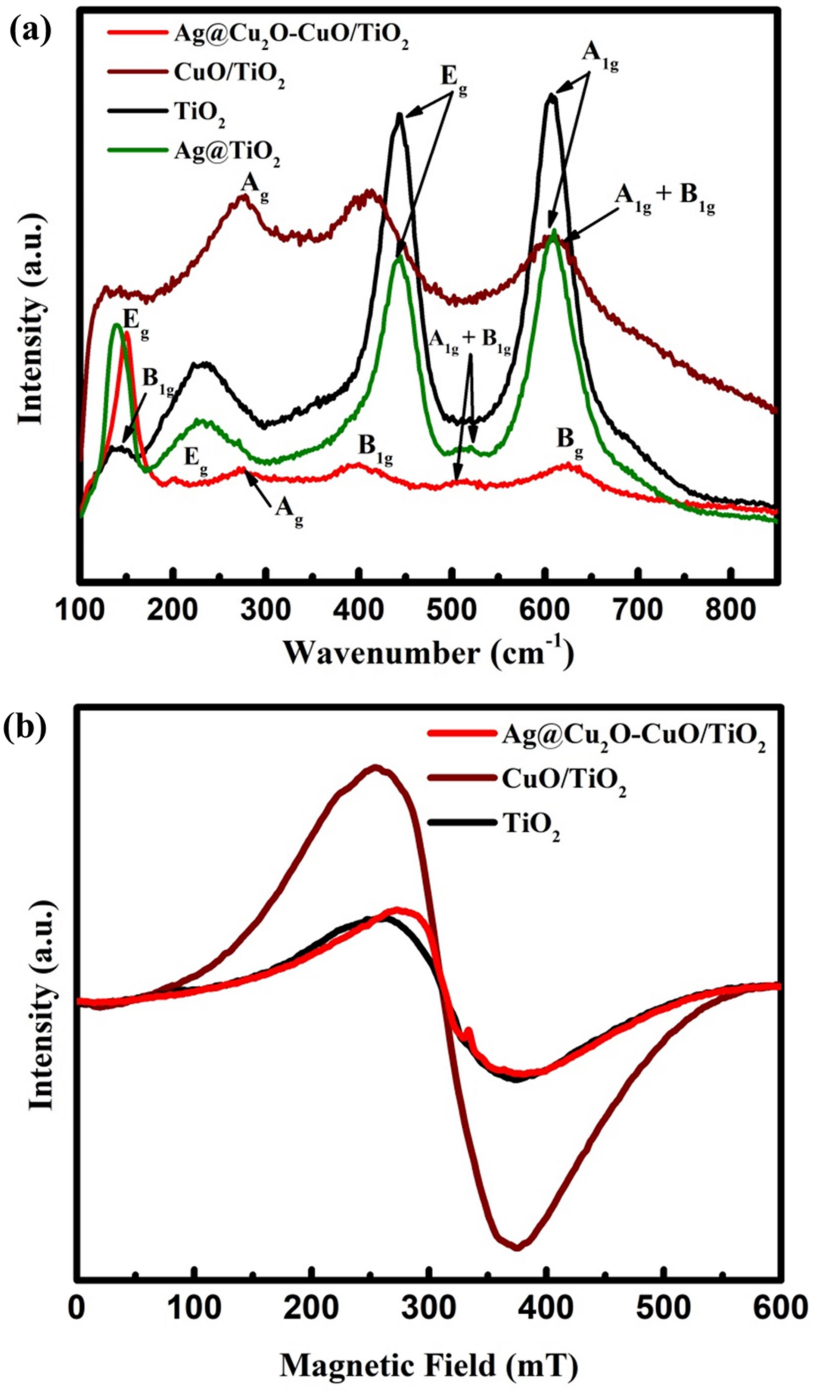

Figure 4.6. (a) Raman, and (b) room temperature ESR spectra, of TiO_2, CuO/TiO_2, and $Ag@Cu_2O$-CuO/TiO_2.

The photoluminescence (PL) measurement provides crucial information about the separation, trapping, and migration of the photoexcited electron holes. Figure 4.7 shows the room temperature PL spectra of TiO_2, CuO, CuO/TiO_2, and $Ag@Cu_2O$-CuO/TiO_2 at the excitation wavelength of 320 nm.

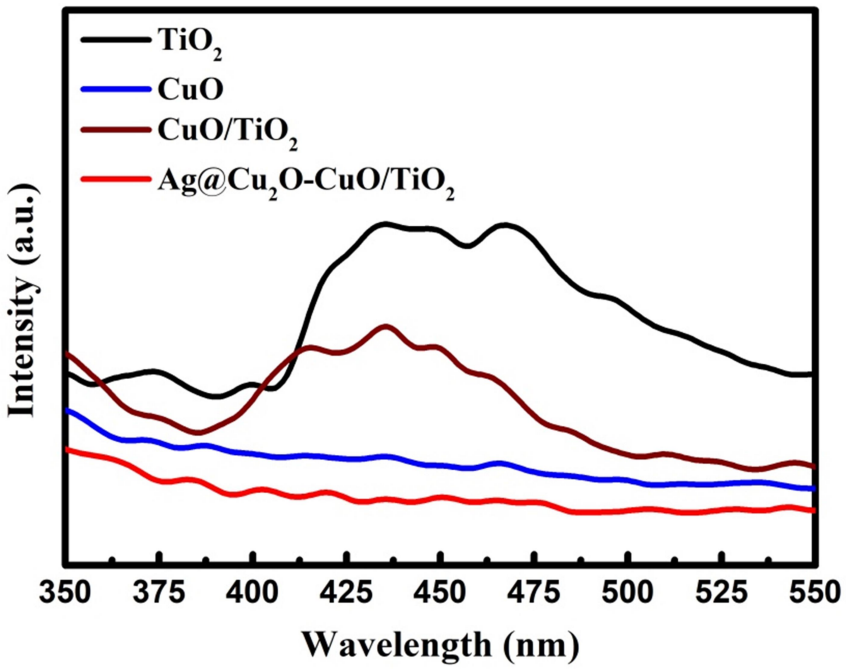

Figure 4.7. Photoluminescence spectra of TiO_2, CuO, CuO/TiO_2, and $Ag@Cu_2O$-CuO/TiO_2.

The pristine TiO_2 and CuO/TiO_2 show emission spectra in a wide wavelength range from 400 to 550 nm, which arises due to the self-trapped excitons, oxygen vacancies, and surface states [28]. However, in the case of CuO, no discernible peaks with significant intensity are detectable. It can be observed that the resultant PL emission spectrum of CuO/TiO_2 is significantly quenched compared to TiO_2, which implies a substantial decrease in the recombination of electron-hole pairs. This is because the photogenerated electrons in the conduction band (CB) of TiO_2 migrate to the CB of CuO. The emission peak located at around 419 and 415 nm in TiO_2 and CuO/TiO_2 respectively, is attributed to the band edge emission corresponding to the bandgap of TiO_2 eV [29]. The emission peaks produced at 434 and 466 nm are attributed to the intrinsic structural defects and the surface oxygen vacancies, respectively [28]. Additionally, the peak detected at 443 nm may be originating from

the self-trapped excitons in TiO_6 octahedra [30]. Notably, the PL emission of $Ag@Cu_2O$-CuO/TiO_2 was further quenched to extremely low intensity, indicating the efficient electron-hole separation and increased lifetime of the carriers. The heterojunction Cu_2O-CuO/TiO_2 and the Schottky junction created with metallic Ag are responsible for facilitating charge separation and transfer through the interfaces.

4.3.3. XPS analysis

XPS was used to study the chemical and electronic states of the prepared catalysts. Figure 4.8(a) depicts the complete scanning spectra of TiO_2, CuO, CuO/TiO_2, and $Ag@Cu_2O$-CuO/TiO_2, revealing the presence of the key components C, Ti, O, Ag, and Cu. The signal of carbon appearing at binding energy (BE) 284.8 eV is due to the presence of adventitious carbon [31].

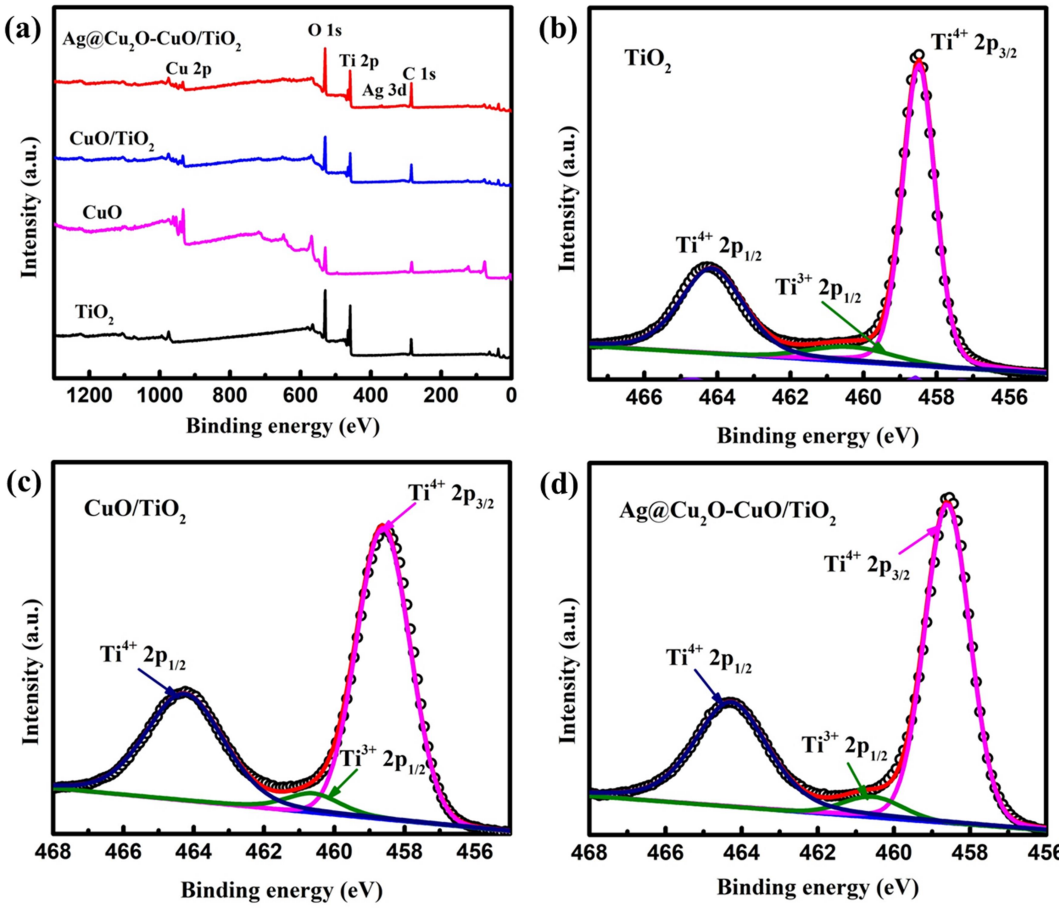

Figure 4.8. (a) XPS measurements (full survey profile) of various catalysts. XPS peak fitting: Ti 2p spectra of (b) TiO_2, (c) CuO/TiO_2, and (d) $Ag@Cu_2O$-CuO/TiO_2.

The entire survey XPS spectra of the counterparts Ag@TiO_2 and Ag@CuO are also displayed with the key elements Ag, Ti, Cu, O, and C, shown in Figure 4.9. The characteristic Ti 2p XPS spectra of TiO_2, CuO/TiO_2, and Ag@Cu_2O-CuO/TiO_2 are presented in Figure 4.8(b), (c), and (d), respectively. The well-resolved Ti spectra of TiO_2 show two distinct peaks at BE 458.5 and 464.1 eV, which correspond to the Ti ($2p_{1/2}$) and Ti ($2p_{3/2}$) doublets, respectively, reveal the existence of the Ti^{4+} oxidation state [32-34]. Similarly, the Ti 2p doublets are observed at BE 458.6 and 464.3 eV for both CuO/TiO_2 and Ag@Cu_2O-CuO/TiO_2. The Ti 2p spectra were deconvoluted into three peaks. For the pristine TiO_2 sample, the deconvoluted peaks are located at 458.5, 460.3, and 464.1 eV (shown in Figure 4.8(b)). The peak at 460.3 eV represents the Ti^{3+} ($2p_{1/2}$) oxidation state [32, 35]. The XPS peaks are found to be shifted to 458.6, 460.6, and 464.3 eV in CuO/TiO_2 and Ag@Cu_2O-CuO/TiO_2. The larger XPS peak fit area owing to the Ti^{3+} ($2p_{1/2}$) state in CuO/TiO_2 (Figure 4.8(c)) and Ag@Cu_2O-CuO/TiO_2 (Figure 4.8(d)) implies the formation of additional oxygen vacancies.

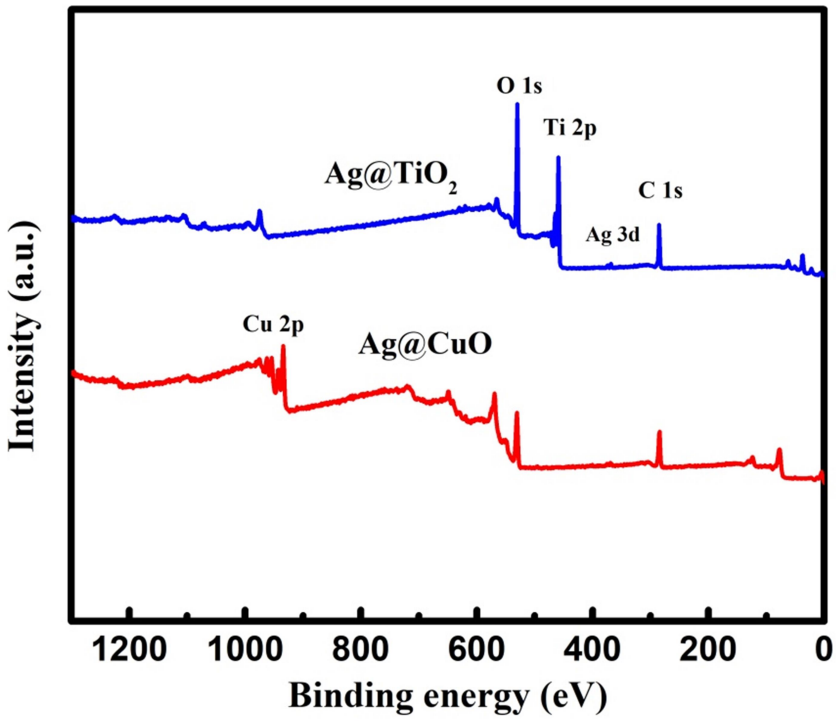

Figure 4.9. XPS spectra of Ag@CuO and Ag@TiO_2 (full survey profile).

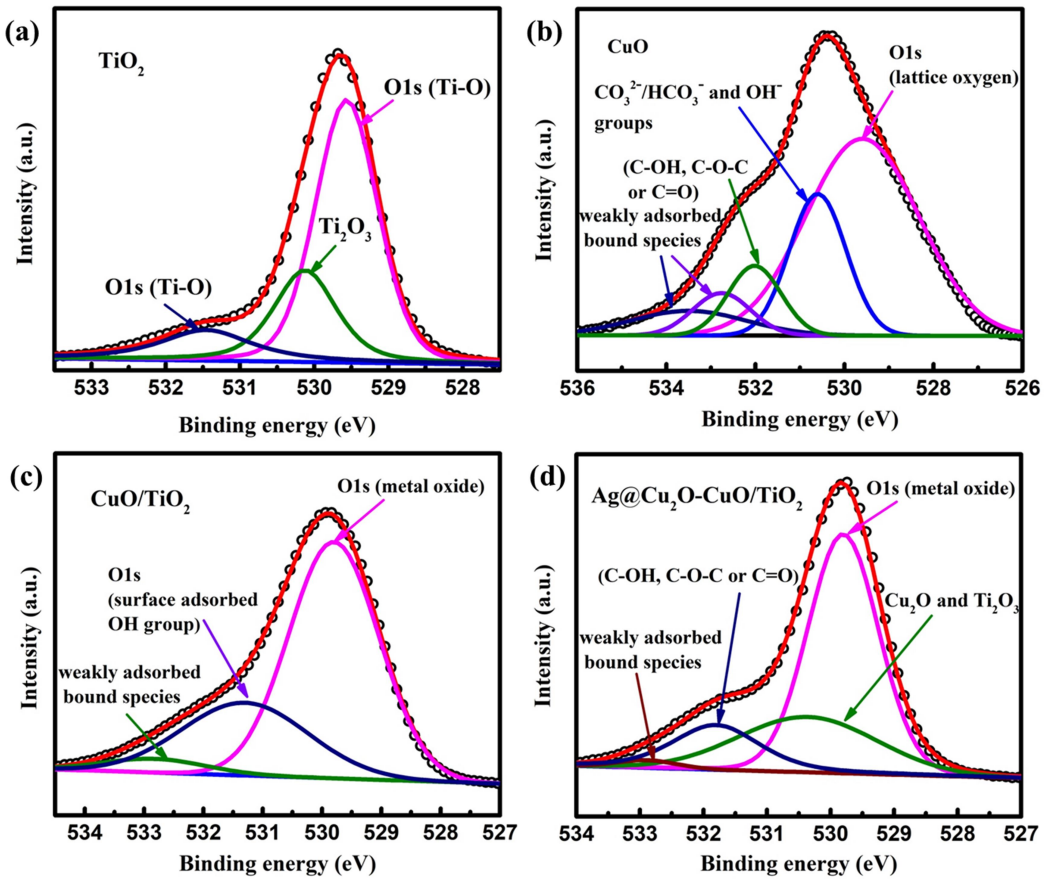

Figure 4.10. XPS peak fitting: O 1s spectra of (a) TiO_2, (b) CuO, (c) CuO/TiO_2, and (d) $Ag@Cu_2O\text{-}CuO/TiO_2$.

The high-resolution O 1s XPS measurements of the prepared photocatalysts are presented in Figure 4.10. In pristine TiO_2, the peaks at BE 529.5, 530.1, and 531.5 eV are attributable to lattice-oxygen, Ti_2O_3, and surface adsorbed O_2 (Figure 4.10(a)) [32, 36-37]. Figure 4.10 (b), (c) and (d) display the fitted O 1s peaks of CuO, CuO/TiO_2 and $Ag@Cu_2O\text{-}CuO/TiO_2$, respectively. As shown in Figure 4.10(b), the O 1s spectra of CuO were deconvoluted with five peaks with binding energy positions 529.6, 530.6, 532.0, 532.7, and 533.5 eV. The peak located at the lowest binding energy of 529.6 eV is allocated to the lattice oxygen of the CuO structure [38-40]. The peak located at 530.6 eV can be assigned to the CO_3^{2-}/HCO_3^- and OH^- groups [41].

The deconvoluted XPS peak at 532.0 eV corresponds to the weakly oxidized carbon species [41, 42] and the peaks at 532.7 and 533.5 eV agree with the binding energy positions where weakly bound species are adsorbed [41, 43-44]. For CuO/TiO_2,

the deconvoluted O 1s peak at 529.8 eV signifies the lattice-O of CuO and/or TiO_2 [36, 37, 43], while the peak at 531.3 and 532.8 eV are due to surface adsorbed OH group and weakly adsorbed bound species [35-38, 41]. Similarly, the fitted O 1s peaks of the sample Ag@Cu_2O-CuO/TiO_2 at 529.8, 530.3, 531.8, and 532.9 eV are ascribed to lattice-O^{2-} of CuO and/or TiO_2, Ti_2O_3 or (lattice- O^{2-} of Cu_2O), weakly oxidized carbon species and adsorbed bound species, respectively [32-34, 37, 38, 41, 43].

Figure 4.11(a-c) illustrates the high-resolution Cu 2p XPS measurements of CuO, CuO/TiO_2, and Ag@Cu_2O-CuO/TiO_2. In CuO, the Cu 2p spectra show two distinct peaks at BE 933.8 and 953.7 eV corresponding to the Cu^{2+} state of CuO. Similarly, the Cu $2p_{3/2}$ and Cu $2p_{1/2}$ doublet was observed at 933.5 and 953.5 eV in CuO/TiO_2 [39, 41, 44-45].

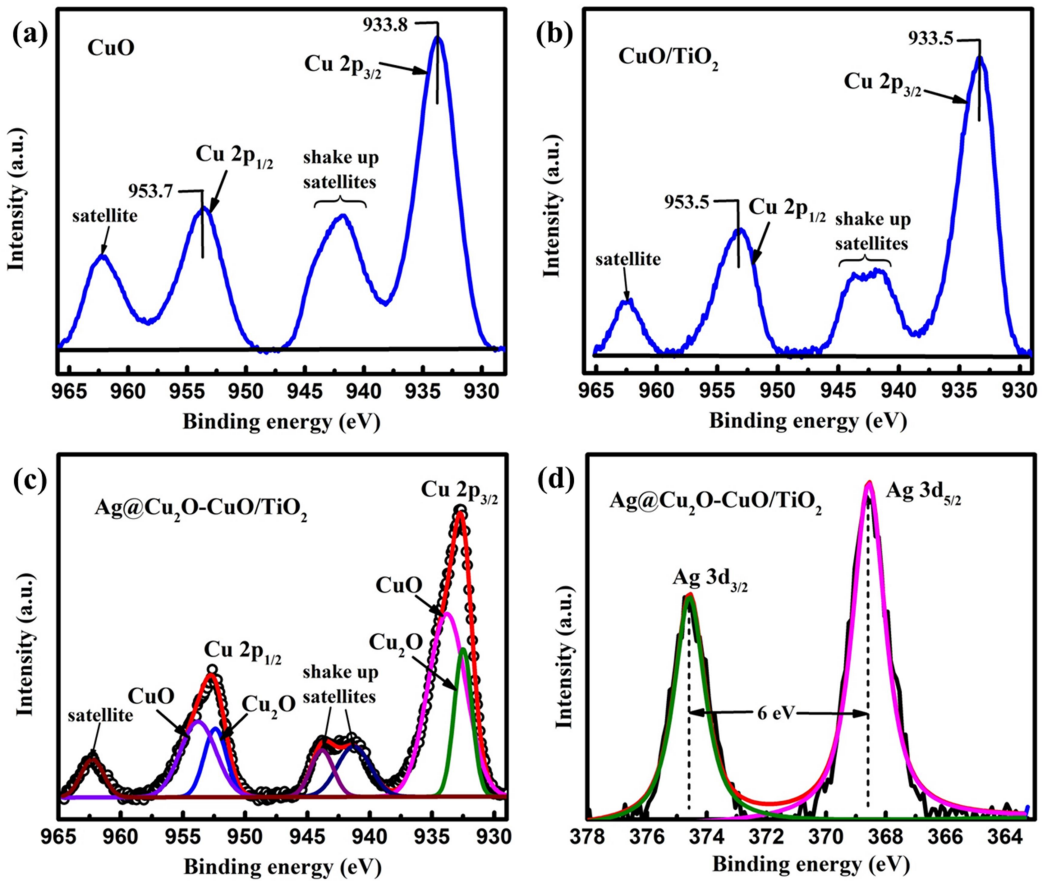

Figure 4.11. XPS peak fitting Cu 2p spectra of (a) CuO, (b) CuO/TiO_2, (c) Ag@Cu_2O-CuO/TiO_2, and (d) XPS scanning of Ag 3d.

In addition, the peaks located at BE 962.2 and 962.4 eV in CuO and CuO/TiO_2, respectively, are related to the typical CuO satellite peaks. The peaks in the binding energy range of 940-945 eV in CuO are known as shake-up satellite peaks (Figure 4.11(a)) [39, 45, 46-49].

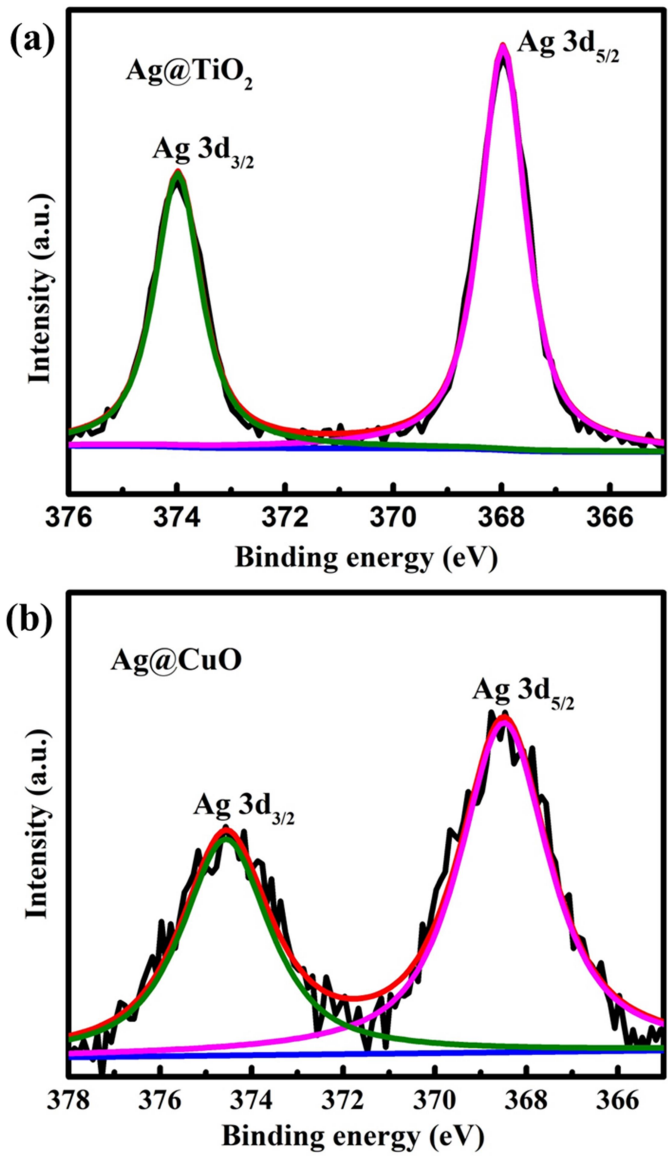

Figure 4.12. Ag 3d XPS spectra of (a) Ag@TiO_2, and (b) Ag@CuO.

However, in Ag@Cu_2O-CuO/TiO_2, the Cu 2p spectrum can be fitted with seven peaks at B.E. 932.5, 933.8, 941.3, 943.8, 952.4, 953.8 and 962.3 eV (Figure 4.11(c)). The peaks at 933.8 and 953.8 eV are attributed to $2p_{3/2}$ and $2p_{1/2}$ peaks of Cu^{2+}. Notably, the additional peaks at 932.5 and 952.4 eV representing Cu $2p_{3/2}$ and Cu $2p_{1/2}$

peaks suggest the presence of Cu_2O (Cu^{1+} oxidation state) in Ag@Cu_2O-CuO/TiO_2 [38, 45, 46, 50, 51]. This result validates the findings of the Raman and ESR studies.

The ratio of the area of Cu $2p_{3/2}$ peak for Cu_2O and CuO in the XPS spectra of Ag@Cu_2O-CuO/TiO_2 was calculated to be 10:27, and the ratio of the area of Cu $2p_{1/2}$ for the same samples was found to be 10:18 showing that CuO is larger in quantity than Cu_2O. The areas of shake-up satellites and satellite peaks are decreased in Ag@Cu_2O-CuO/TiO_2, which could be due to the presence of Ag that retards the complete transformation from Cu_2O to CuO. Furthermore, the well-resolved XPS spectrum of Ag 3d of the Ag@Cu_2O-CuO/TiO_2 photocatalyst is shown in Figure 4.11(d). The Ag 3d doublet at 368.5 ($3d_{5/2}$) and 374.5 ($3d_{3/2}$) eV is due to the spin-orbit splitting, and exhibits an energy separation of 6.0 eV, indicating the presence of metallic Ag [52-54]. Similar results were evidenced in Ag@TiO_2 and Ag@CuO, shown in Figures 4.12 (a) and (b), respectively.

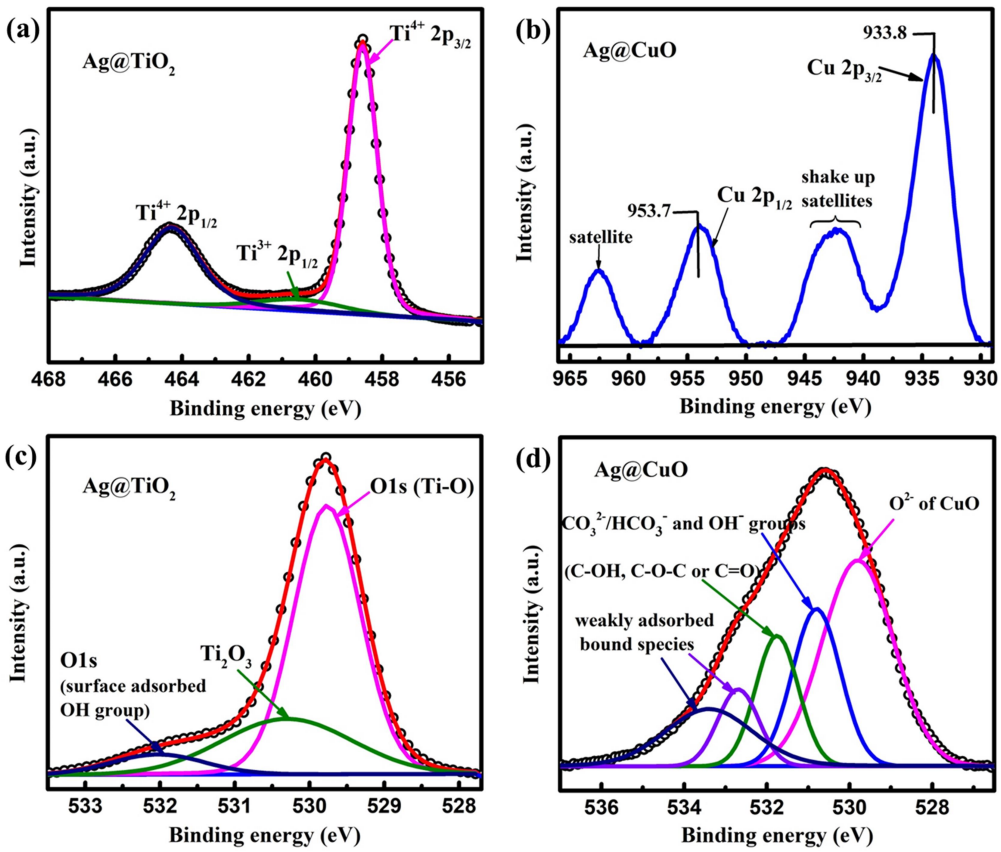

Figure 4.13. XPS spectra of Ag@CuO and Ag@TiO_2 (a) Ti 2p spectra, (b) Cu 2p spectra, and (c-d) O 1s spectra.

Figure 4.13 shows the (Ti 2p, O 1s, Cu 2p) XPS spectrum of Ag@TiO_2 and Ag@CuO. The Ti 2p XPS spectrum of Ag@TiO_2 was deconvoluted into three peaks at BE 458.6, 460.5, and 464.4 eV, shown in Figure 4.13(a). The high-resolution Cu 2p spectrum of the Ag@CuO sample as shown in Figure 4.13(b) reveals only the Cu^{2+} oxidation state. The fitted O 1s XPS peaks of Ag@TiO_2 and Ag@CuO counterparts are displayed in Figures 4.13 (c), and (d). respectively.

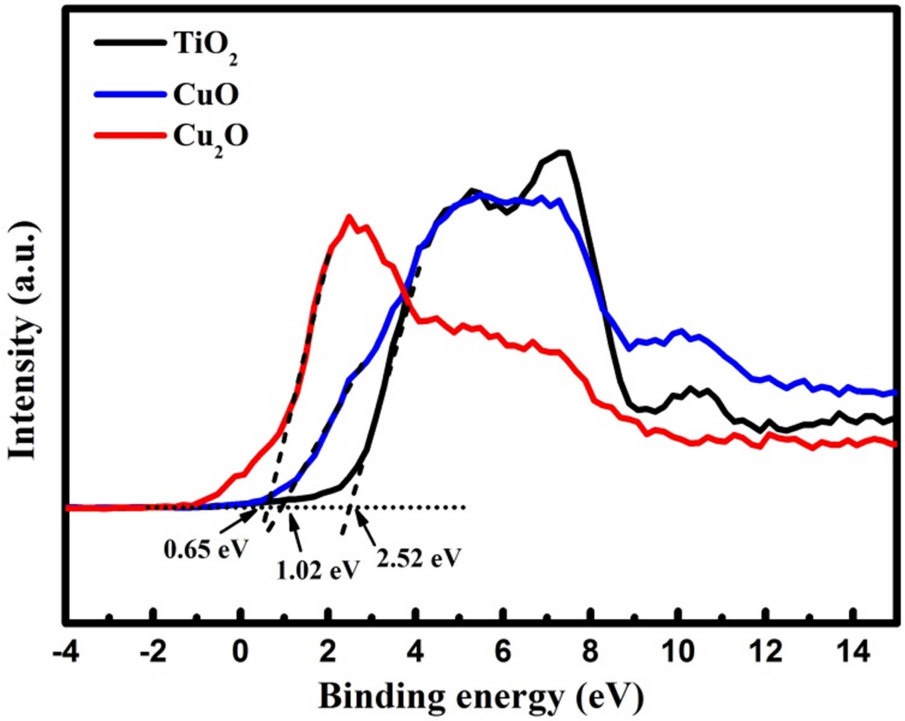

Figure 4.14. Valence band XPS spectra of TiO_2, CuO, and Cu_2O.

The valence band XPS spectra of TiO_2, CuO, and Cu_2O were recorded to determine the valence band maximum (VBM) and comprehend the band edge positions of the heterojunctions [55]. The VBM of pristine TiO_2 was found to be 2.52 eV, determined by linear extrapolation of the curve as shown in Figure 4.14. Likewise, the VBM of CuO and Cu_2O was calculated to be 1.02 eV and 0.65 eV, respectively. Thus, considering the bandgap value obtained from the Tauc plot (shown in Figure 4.4(b)), the conduction band minimum (CBM) of the photocatalysts were estimated to be -0.5, -0.45, and -1.36 eV for TiO_2, CuO and Cu_2O, respectively.

4.3.4. FE-SEM and TEM analysis

The surface morphologies of Ag, TiO_2, CuO, CuO/TiO_2, and $Ag@Cu_2O$-CuO/TiO_2 were characterized by FE-SEM, shown in Figure 4.15(a-f).

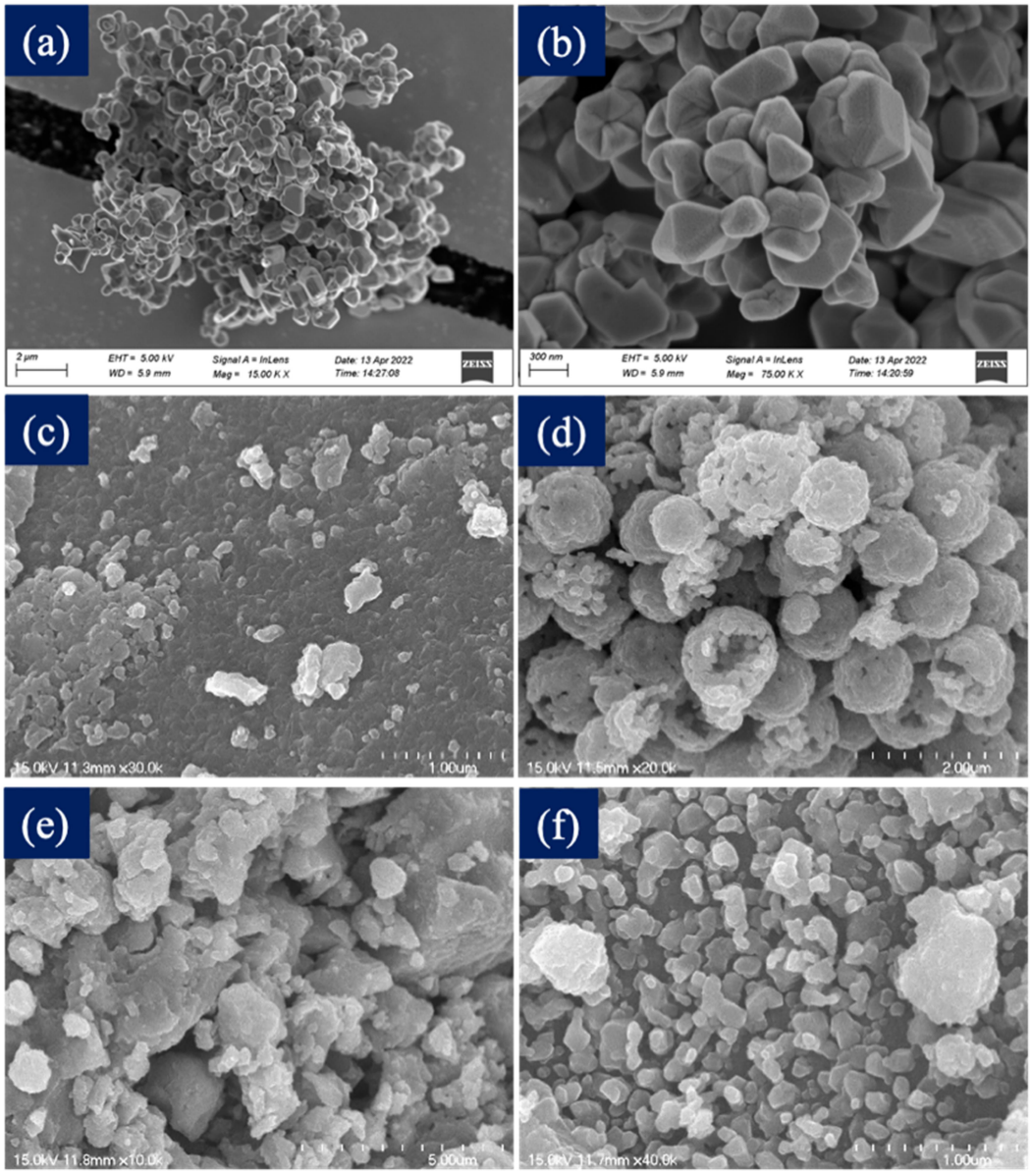

Figure 4.15. FE-SEM image of (a-b) Ag, (c) TiO_2, (d) CuO, (e) CuO/TiO_2, and (f) $Ag@Cu_2O$-CuO/TiO_2.

The formation of the bulbous branched structure of Ag is displayed in Figure 4.15(a-b) at different magnifications. The TiO_2 nanoparticles are observed to be agglomerated, with an average size of 50 nm (Figure 4.15(c)). The SEM micrograph of pure CuO shows a spherical structure of sizes 500 to 900 nm (shown in Figure 4.15(d)).

However, this spherical shape is no longer observed in CuO/TiO_2 and $Ag@Cu_2O$-CuO/TiO_2, which could be due to the higher amount of TiO_2 matrix than CuO. Similar morphology was observed in CuO/TiO_2 and $Ag@Cu_2O$-CuO/TiO_2, as shown in Figures 4.15 (e) and (f).

In addition, the TEM images of Ag, TiO_2, CuO/TiO_2, and $Ag@Cu_2O$-CuO/TiO_2 were analyzed to obtain further morpho-structural information. The structure of Ag is shown in Figure 4.16(a).

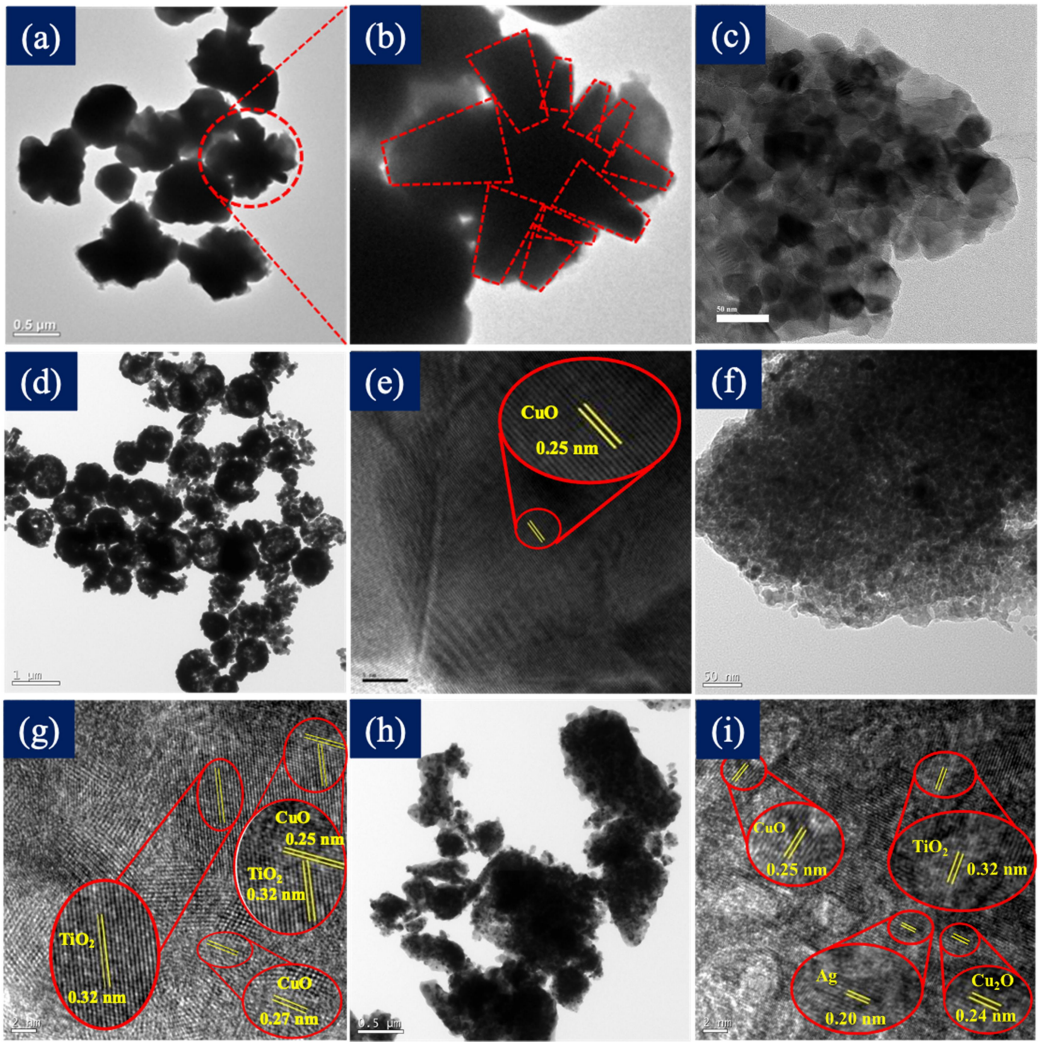

Figure 4.16. TEM and HR-TEM images of (a-b) Ag, (c) TiO_2, (d-e) CuO, (f-g) CuO/TiO_2, and (h-i) $Ag@Cu_2O$-CuO/TiO_2.

The magnified view of Ag particles is displayed in Figure 4.16(b) with highlighted dotted lines. A uniform distribution of the spherical-shaped pure CuO was evidenced with average sizes of 0.9 µm, shown in Figure 4.16(d). The TEM image of

TiO_2, CuO/TiO_2, and $Ag@Cu_2O$-CuO/TiO_2 are presented in Figure 4.16 (c), (f), and (h), respectively, and show similar morphological characteristics. The obtained size of the TiO_2 nanoparticles ranged from 30 to 50 nm. The interplanar spacing (*d*) of CuO, calculated from the HR-TEM micrograph, shown in Figure 4.16(e), was found to be 0.25 nm. The HR-TEM of CuO/TiO_2 in Figure 4.16(g), reveals the presence of two different interplanar spacings, 0.25 and 0.32 nm, which correspond to CuO and TiO_2, respectively. Furthermore, the obtained interplanar spacings 0.2, 0.24, 0.25, and 0.32 nm in the $Ag@Cu_2O$-CuO/TiO_2 sample (shown in Figure 4.16(i)), indicated the existence of Ag, Cu_2O, CuO, and TiO_2, respectively.

4.3.5. Photocatalytic degradation kinetics

To evaluate the photocatalytic activity of the photocatalysts, the kinetic study of MB degradation was performed. Figure 4.17(a) illustrates the degradation profile of MB from 0 to 60 min irradiation of visible light. A maximum degradation was shown by $Ag@Cu_2O$-CuO/TiO_2 with a degradation percentage of 83%, while the CuO/TiO_2, CuO, and TiO_2 photocatalysts exhibited 26, 6.4, and 5.9%, respectively. The rate of degradation of MB was calculated from ln C/C_o vs. time graph as plotted in Figure 4.17(b). The degradation followed pseudo-first-order kinetics with a good regression coefficient. The degradation rate by $Ag@Cu_2O$-CuO/TiO_2 photocatalyst was found 26.5 times higher than the pure TiO_2. Table 4.1 displays the calculated rate constants of MB degradation by different photocatalysts and regression coefficients of the linear fit. It was observed that the CuO/TiO_2 photocatalyst also exhibits a significant improvement in MB degradation compared to pure TiO_2. This enhancement is likely due to the electron-hole separation due to the built-in electric field at the interface that prolongs the lifetime of charge carriers for photocatalytic reactions [56, 57]. Notably, the activity was further enhanced by $Ag@Cu_2O$-CuO/TiO_2 photocatalyst. The SPR effect of branched Ag nanostructure amplifies the localized electric field in their vicinity, increasing charge carrier generation and facilitating effective separation between them [1]. Due to the shape effect of the plasmonic nanostructures, the particular branched structure of Ag exhibits low symmetry, allowing for extensive absorption over the visible spectrum. [13-14, 58]. In addition, the Ag nanoparticle acts as an electron source, which promotes the electron injection into the CB of the semiconductors under visible light illumination [1].

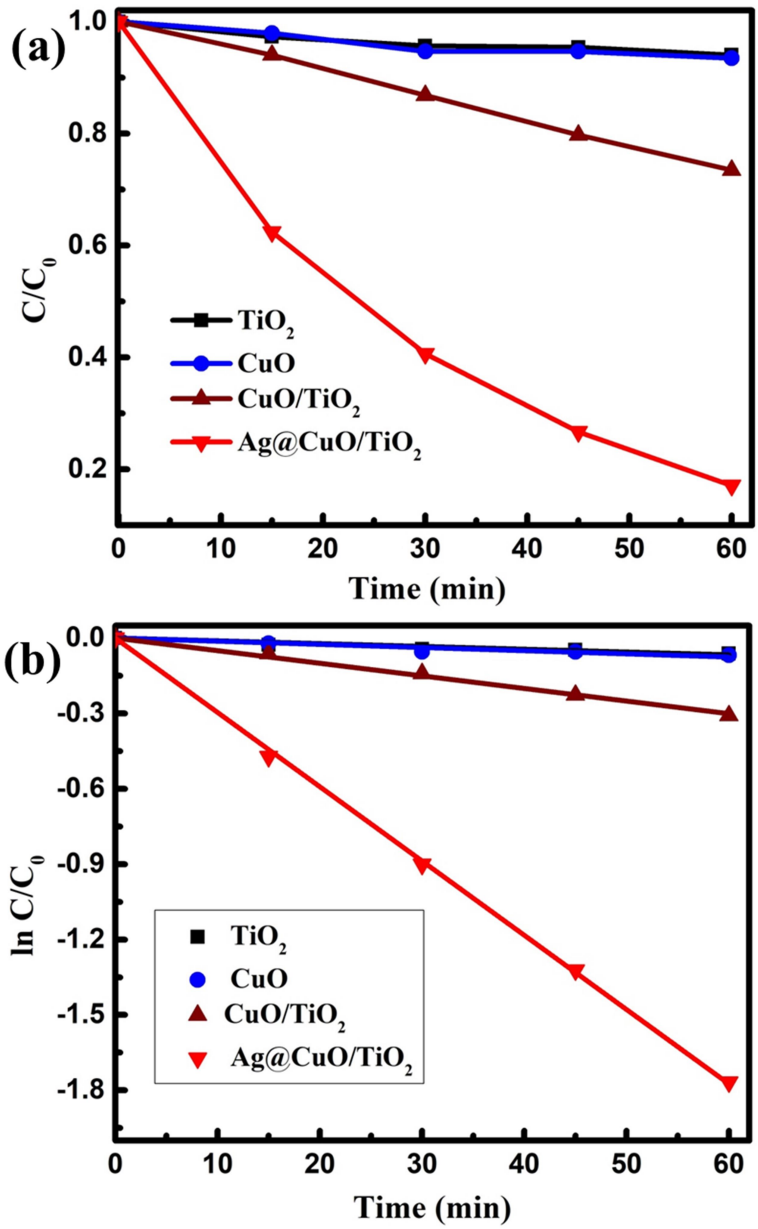

Figure 4.17. (a) Photocatalytic degradation profile (C/C_o vs. time) of MB under visible light using different photocatalysts, (b) ln C/C_o vs. time plot to determine the rate constant.

The absorption spectra of MB degradation using various photocatalysts are shown in Figure 4.18(a-d). The maximum absorption of the MB dye was recorded at wavelength 664 nm. The degradation trend and the rate constant determination of the counterparts $Ag@TiO_2$ and Ag@CuO are displayed in Figure 4.19(a-b). The rate constant of $Ag@TiO_2$ and Ag@CuO were calculated as 0.004 min^{-1} and 0.003 min^{-1}.

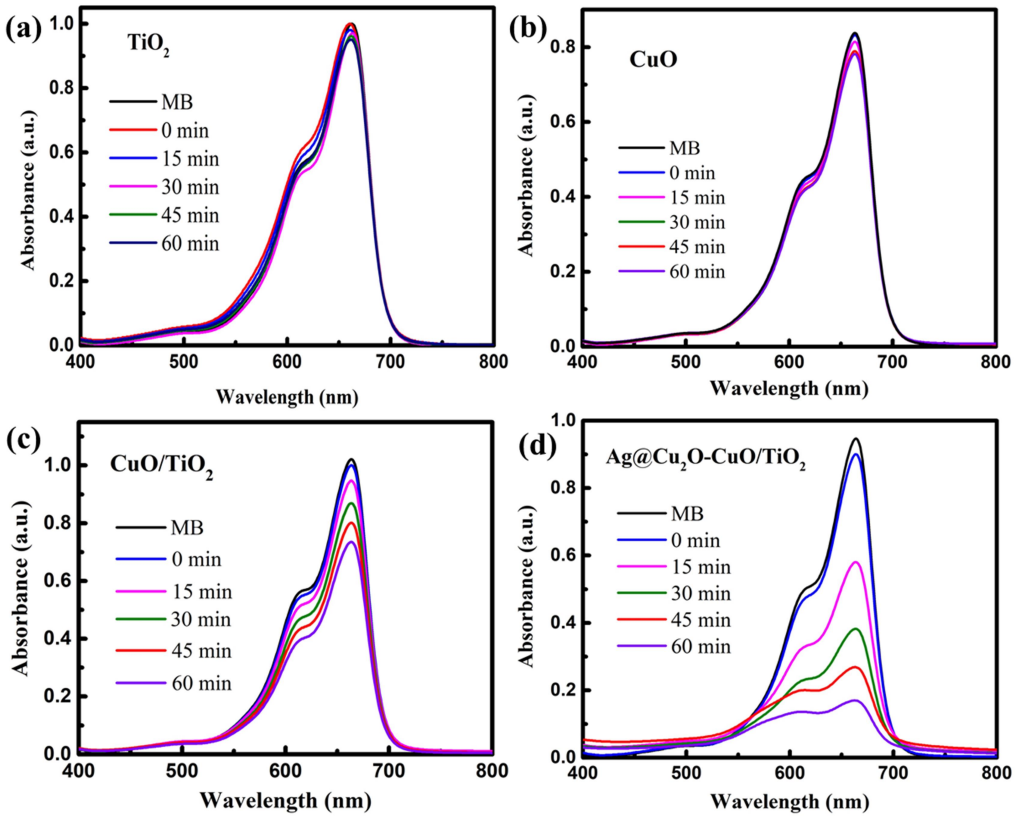

Figure 4.18. Absorption spectra of MB degradation with time using (a) TiO_2, (b) CuO, (c) CuO/TiO_2, and (d) $Ag@Cu_2O\text{-}CuO/TiO_2$.

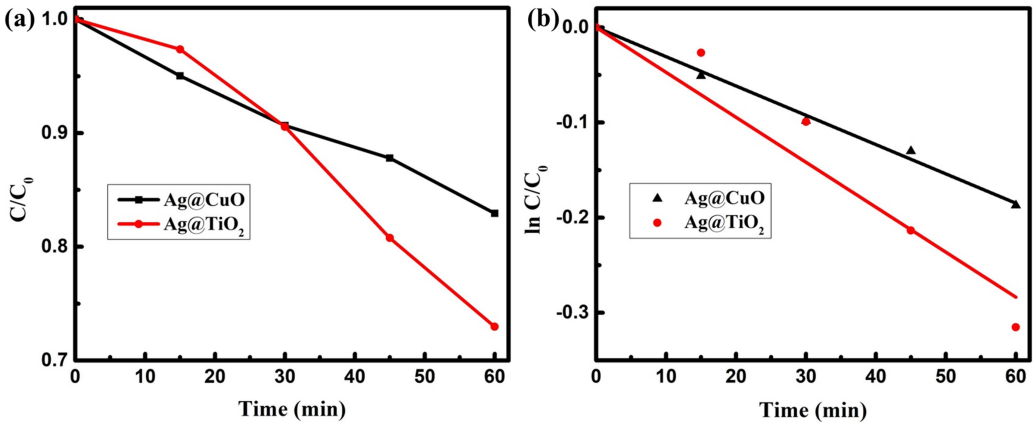

Figure 4.19. (a) Photocatalytic degradation profile (C/C_o vs. time) of MB under visible light using $Ag@TiO_2$ and Ag@CuO, (b) ln C/C_o vs. time plot to determine the rate constant.

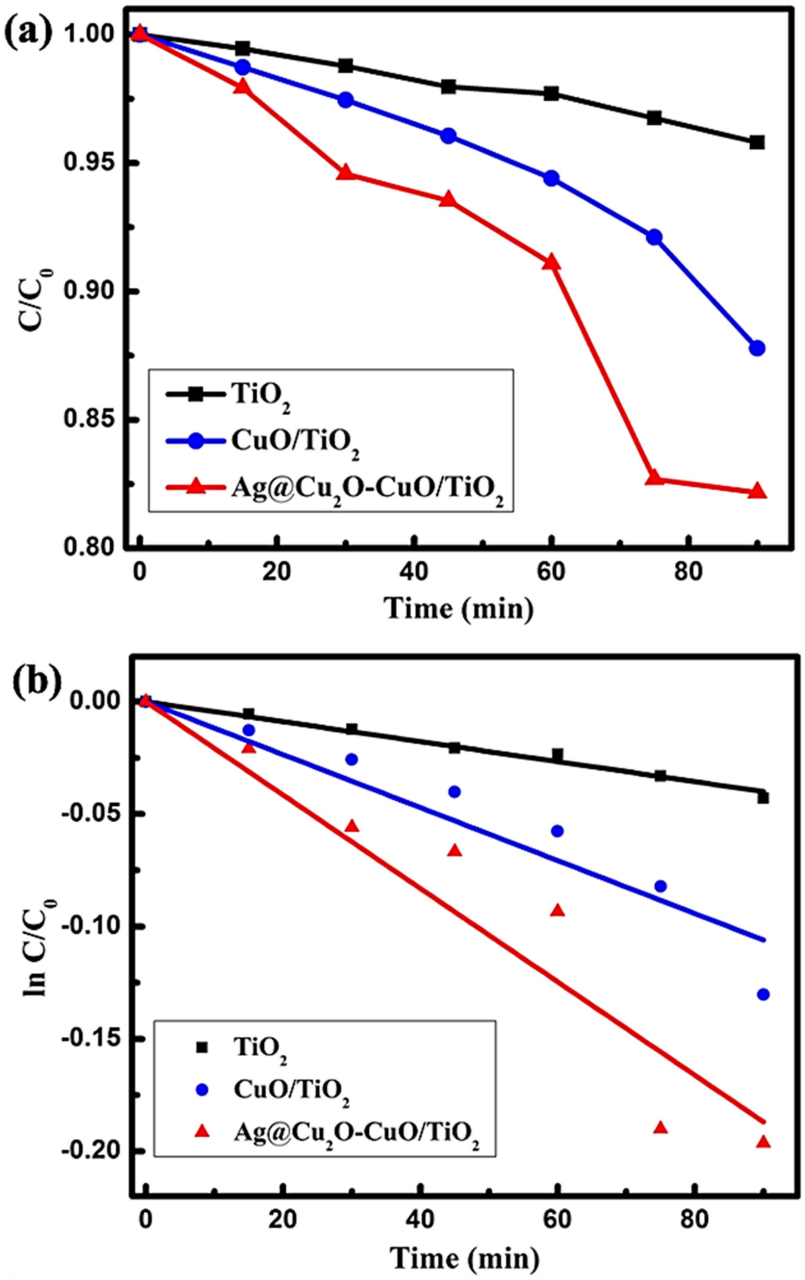

Figure 4.20. (a) Photocatalytic degradation profile (C/C_o vs. time) of phenol under visible light using TiO_2, CuO/TiO_2, and $Ag@Cu_2O$-CuO/TiO_2, and (b) ln C/C_o vs. time plot to determine the rate constant.

In addition, the degradation of phenol using the photocatalysts was performed under a similar experimental setup and light illumination as discussed in Chapter 2. Figure 4.20 illustrates the degradation profile and determination of the rate constant of

phenol degradation using TiO_2, CuO/TiO_2 and $Ag@Cu_2O$-CuO/TiO_2 photocatalyst. Pristine TiO_2 showed negligible degradation of phenol. However, a small enhancement in photocatalytic activity was observed with the CuO/TiO_2 photocatalyst, while further enhancement in the activity was achieved by $Ag@Cu_2O$-CuO/TiO_2. The degradation rate of phenol using $Ag@Cu_2O$-CuO/TiO_2 was found to be 5 times higher compared to TiO_2.

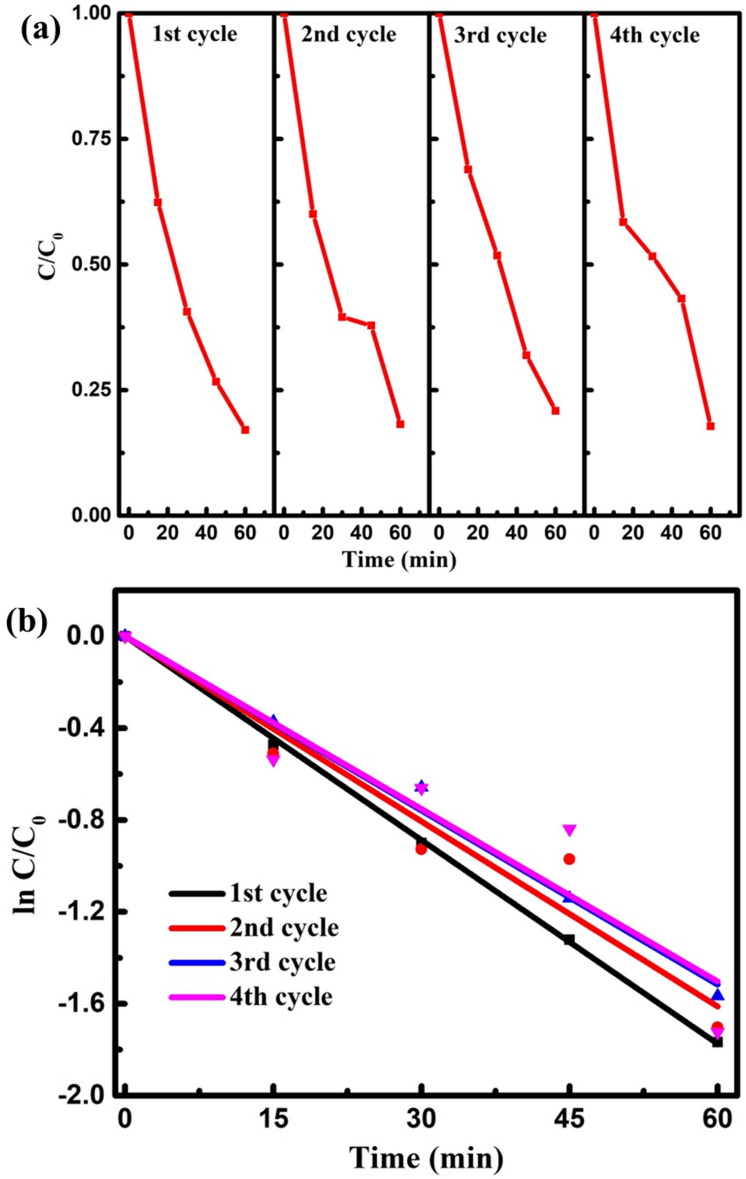

Figure 4.21. (a) Repeatability test of $Ag@Cu_2O$-CuO/TiO_2 photocatalyst, and (b) ln C/C_o vs. time plot to determine the rate constant.

Table 4.1. Rate of degradation of MB using different photocatalysts under visible light.

Photocatalyst	Rate constant of MB degradation (min^{-1})	Regression coefficient (R^2)
TiO_2	0.001	0.961
CuO	0.001	0.959
CuO/TiO_2	0.005	0.997
$Ag@Cu_2O$-CuO/TiO_2	0.029	0.999

The repeatability test was carried out to evaluate the stability of the primary photocatalyst $Ag@Cu_2O$-CuO/TiO_2 under a similar experimental set-up and the light source (as discussed in Section 2.5.1), and is shown in Figure 4.21(a). The repeatability test was conducted over four cycles of 60 min each. After each cycle, the remanent MB concentration was made equal to the initial value (at 0 min) before initiating the next photocatalysis cycle. The fall in the photocatalytic activity after the fourth cycle was extremely minimal, displayed in Figure 4.21(b) (less than 15%), indicating the high stability and robustness of the photocatalyst.

4.3.6. Active radical quenching experiments

To understand the active species involved in the degradation of MB, free radical quenching experiments were conducted for the main photocatalyst $Ag@Cu_2O$-CuO/TiO_2, shown in Figure 4.22(a). The major reactions that occur in the photocatalytic process are shown in equation (1.1-1.12) in Chapter 1. It was observed that there is a significant drop in MB degradation when the SN (e^- quencher), LH ($^1O_2$ quencher), and AO (h^+ quencher) were introduced, in the order SN > LH > AO, shown in Figure 4.22(b). This result indicates the major participation of e^-, $^1O_2$ and h^+ in the degradation process. The calculated rate constants are shown in Table 4.2. On the other hand, there is only a small decline in the degradation with the addition of BQ ($^{\bullet}O_2^-$ quencher) and IPA ($^{\bullet}OH$ quencher), up to 4.3% and 1%, respectively. However, to ensure the role of $^{\bullet}O_2^-$ and $^{\bullet}OH$ radicals, a double-quenching test was performed using BQ and IPA simultaneously. Clearly, a substantial drop in the degradation was observed in double-

quenching, which indicates that $^{\bullet}O_2^-$ and $^{\bullet}OH$ radicals are produced abundantly by e^- and h^+ and therefore individual quenching is not sufficient using BQ and IPA [59].

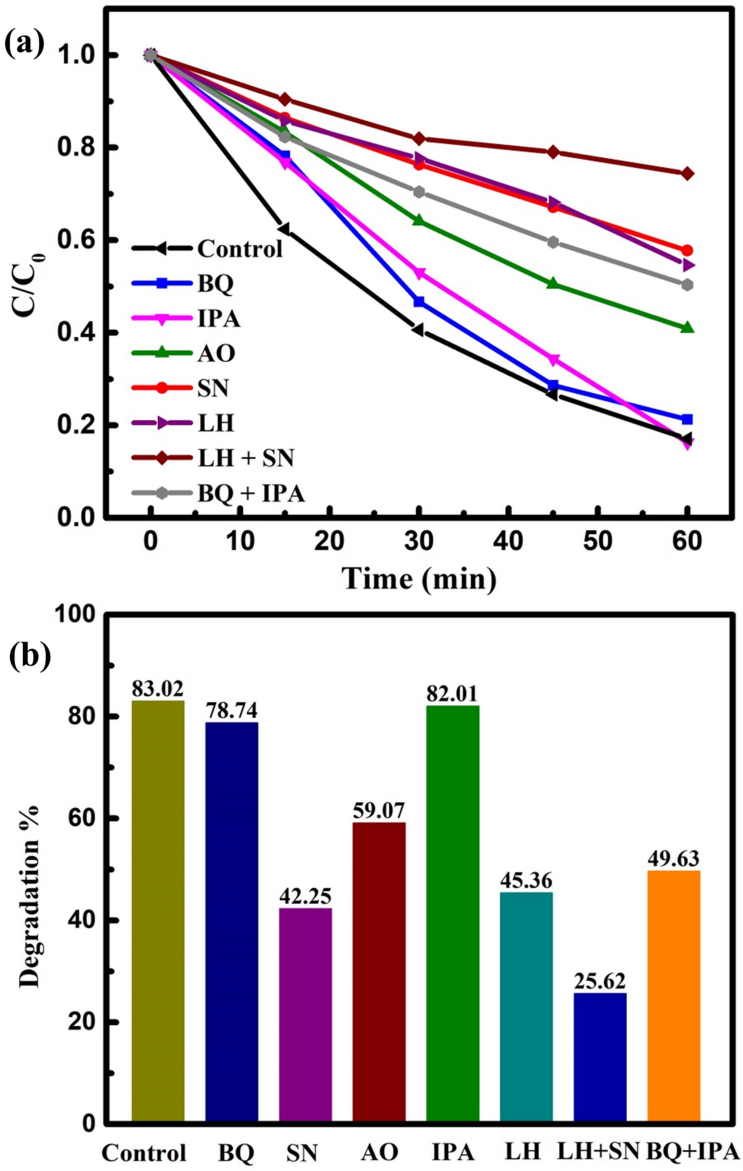

Figure 4.22. (a) Photocatalytic degradation of MB and (b) degradation percent by $Ag@Cu_2O$-CuO/TiO_2 photocatalyst with various scavenging agents.

Table 4.2. Rate constants, quenching agents and amount, and active radicals.

Quenching agent	Amount	Active radical (s)	Rate constant (min^{-1})
SN	4mM	e^-	0.009
LH	0.5 mM	$^1O_2$	0.009

AO	4mM	h^+	0.014
BQ	0.5mM	$^{\bullet}O_2^-$	0.026
IPA	1mL	$^{\bullet}OH$	0.026
BQ + IPA	0.5mM + 1mL	$^{\bullet}O_2^-$ and $^{\bullet}OH$	0.009
SN+LH	4mM+0.5 mM	e^- and $^1O_2$	0.005

It can be speculated that, during $^{\bullet}O_2^-$ quenching by BQ, the production of $^{\bullet}OH$ (by both e^- and h^+) is sufficient to take part in the degradation reaction and therefore no significant decline in the degradation can be observed. Likewise, $^{\bullet}OH$ quenching by IPA was compensated by $^{\bullet}O_2^-$ production. In addition, the double-quenching experiment using LH and SN demonstrates the lowest degradation of MB, implying the active participation of both e^-, and $^1O_2$. Summarily, when the scavenging agent SN and AO capture e^- and h^+, respectively, it prevents the formation of $^{\bullet}O_2^-$, $^{\bullet}OH$, and $^1O_2$, resulting substantial decline in the degradation.

4.3.7. Photocatalytic mechanism and schematic representation

As indicated by valence band XPS analysis and the Tauc plot, the conduction band minimum (CBM) of TiO_2 is situated below the CBM of Cu_2O, whereas the valence band maximum (VBM) of TiO_2 lies much below than that of Cu_2O, forming a Type-II (staggered gap) band alignment between TiO_2 and Cu_2O. Likewise, the CBM and VBM levels of CuO are situated between the CBM and VBM position of TiO_2, resulting in a Type-I (straddling gap) heterojunction. Figure 4.23 illustrates the ternary heterojunction system, where a Type-I heterojunction exists between CuO and TiO_2, while a Type-II heterojunction is present between Cu_2O and TiO_2. The Ag nanoparticles are considered to be in contact with CuO, Cu_2O, and TiO_2. The unique branching shape of the Ag microstructure obtained in this study enables electromagnetic waves to stimulate multiple resonances in the nanoparticles resulting in broad absorption of the visible light spectra [60, 13]. The facets of Ag nanoparticles, revealed from SEM images, can establish excellent contact with CuO and TiO_2, forming a Schottky junction that effectively separates photogenerated charge carriers [61]. When the photocatalyst is illuminated by light, the semiconductors CuO, Cu_2O, and TiO_2 generate electron-hole pairs, and the electrons in the Ag metal exhibit local surface plasmonic resonance. As depicted in Figure 4.23, the photo-excited electrons at the CB of the Cu_2O phase are

initially expected to be transferred to the CB of TiO_2 and subsequently to the CB of CuO [62-64]. On the other hand, the holes generated at the VB of TiO_2 migrate towards VBs of CuO and Cu_2O. However, the holes that are transferred to the VB of Cu_2O are unable to produce reactive species as the VB position is unsuitable for oxidation reactions (indicated with a cross mark in Figure 4.23). Besides, the SPR promotes electron injection from Ag nanoparticles, leading to a higher population of electrons at the conduction bands of TiO_2, CuO, and Cu_2O, which ensures the adequate availability of charge carriers for photocatalytic reactions [1]. These electrons are the outcome of plasmonic excitations induced by the time-dependent electric field of illuminating light in the visible range. Consequently, the photogenerated electrons and holes undergo a large spatial separation, migrate towards the surface of the photocatalyst, and participate in chemical reactions with the adsorbed molecules to produce active radicals [65, 66].

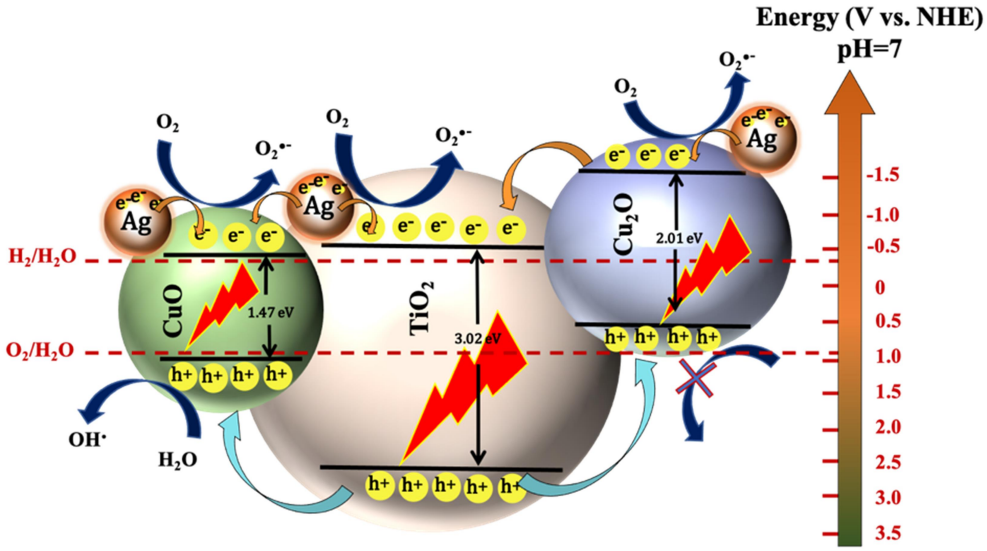

Figure 4.23. Photocatalytic mechanism of Ag@Cu_2O-CuO/TiO_2 photocatalyst: interfacial junctions between CuO-TiO_2-Cu_2O phase.

4.4. Summary

The synthesis of a novel plasmonic-heterojunction photocatalyst (Ag@Cu_2O-CuO/TiO_2) with extensive visible light absorption and high photocatalytic activity has been reported in this chapter. XRD and XPS measurements corroborated the crystalline phases of CuO and TiO_2, chemical compositions, and the presence of metallic Ag. The asymmetrical feature of branched Ag, confirmed in the FE-SEM analysis, results in

SPR induced light absorption across the visible and near-infrared region. The photocatalytic activity of the Ag@Cu_2O-CuO/TiO_2 photocatalyst was found to be 26.5 times higher than the pristine TiO_2 counterpart towards methylene blue degradation without sacrificial reagents. The increased photoactivity of Ag@Cu_2O-CuO/TiO_2 photocatalyst can be attributed to the synergistic impact of reduced electron-hole pair recombination caused by the Cu_2O-CuO/TiO_2 ternary heterojunction, strong visible light absorption, and SPR driven enhanced localized field by Ag. In addition, the presence of the mixed phase of TiO_2 in Ag@Cu_2O-CuO/TiO_2 facilitates interfacial charge separation between the phases. Remarkably, the photocatalyst exhibited exceptional recyclability, indicating its excellent stability and robustness for efficient photocatalytic applications. The current study suggests that the heterojunction-plasmonic nanostructured photocatalyst substantially enhances the photocatalytic efficiency synergistically and shows great potential for dye-contaminated water treatments. The research work presented in this chapter aligns with the objectives outlined in this thesis.

References

1. X. Zhang, Y.L. Chen, R.S. Liu, D.P. Tsai, Plasmonic photocatalysis, Rep. Prog. Phys. 76 (2013) 046401.
2. J. Ji, Z. Li, W. Sun, H. Wang, Thermal annealing induced tunable localized surface plasmon resonance of Au/Ag bimetallic thin film, Chem. Phys. 541 (2021) 111034.
3. C. An, S. Wang, Y. Sun, Q. Zhang, J. Zhang, C. Wang, J. Fang, Plasmonic silver incorporated silver halides for efficient photocatalysis, J. Mater. Chem. A 4 (2016) 4336-4352.
4. M.J. Nalbandian, M. Zhang, J. Sanchez, S. Kim, Y.H. Choa, D.M. Cwiertny, N.V. Myung, Synthesis and optimization of Ag-TiO_2 composite nanofibers for photocatalytic treatment of impaired water sources, J. Hazard. Mater. 299 (2015) 141-148.
5. R. Raji, K.S. Sibi, K.G. Gopchandran, ZnO: Ag nanorods as efficient photocatalysts: Sunlight driven photocatalytic degradation of sulforhodamine B, Appl. Surf. Sci. 427 (2018) 863-875.
6. E.L. Ru, P. Etchegoin, Principles of Surface–Enhanced Raman Spectroscopy: and Related Plasmonic Effects, Elsevier, Oxford, U.K, 2009.

7. P.C. Nagajyothi, S.V. Prabhakar Vattikuti, K.C. Devarayapalli, K. Yoo, J. Shim, T. V. M. Sreekanth, Green synthesis: Photocatalytic degradation of textile dyes using metal and metal oxide nanoparticles-latest trends and advancements, Crit. Rev. Environ. Sci. Technol. 50 (2020) 2617-2723.
8. Y. Tian, T. Tatsuma, Mechanisms and applications of plasmon-induced charge separation at TiO_2 films loaded with gold nanoparticles, J. Am. Chem. Soc. 127 (2005) 7632-7637.
9. Q.P. Zhang, J. Li, M. Xu, Ag decorated ZnO based nanocomposites for visible light-driven photocatalytic degradation: basic understanding and outlook, J. Phys. D: Appl. Phys. 55 (2022) 483001
10. N.L. Gavade, S.B. Babar, A.N. Kadam, A.D. Gophane, K.M. Garadkar, Fabrication of M@Cu_xO/ZnO (M = Ag, Au) heterostructured nanocomposite with enhanced photocatalytic performance under sunlight, Ind. Eng. Chem. Res. 56 (2017) 14489-14501.
11. A. Ramchiary, S.K. Samdarshi, Ag deposited mixed phase titania visible light photocatalyst–Superiority of Ag-titania and mixed phase titania co-junction, Appl. Surf. Sci. 305 (2014) 33-39.
12. Y. Zhu, K. Mimura, M. Isshiki, Oxidation mechanism of Cu_2O to CuO at 600-1050 ^oC, Oxid. Met. 62 (2004) 207-222.
13. Y. Wang, P.H. Camargo, S.E. Skrabalak, H. Gu, Y. Xia, A facile, water-based synthesis of highly branched nanostructures of silver, Langmuir 24 (2008) 12042-12046.
14. M. Rycenga, C.M. Cobley, J. Zeng, W. Li, C.H. Moran, Q. Zhang, D. Qin, Y. Xia, Controlling the synthesis and assembly of silver nanostructures for plasmonic applications, Chem. Rev. 111 (2011) 3669-3712.
15. L. Samet, J.B. Nasseur, R. Chtourou, K. March, O. Stephan, Heat treatment effect on the physical properties of cobalt doped TiO_2 sol–gel materials, Mater. Charact. 85 (2013) 1-12.
16. B.R. Bade, S. Rondiya, S.R. Bhopale, N.Y. Dzade, M.M. Kamble, A. Rokade, M.P. Nasane, M.A. More, S.R. Jadkar, A.M. Funde, Investigation of growth mechanism for highly oriented TiO_2 nanorods: The role of reaction time and annealing temperature, SN Appl. Sci. 1 (2019) 1-13.

17. S. Challagulla, K. Tarafder, R. Ganesan, S. Roy, Structure sensitive photocatalytic reduction of nitroarenes over TiO_2, Sci. Rep. 7 (2017) 1-11.
18. J. Singh, K. Sahu, S. Mohapatra, Thermal annealing induced evolution of morphological, structural, optical and photocatalytic properties of Ag-TiO_2 nanocomposite thin films, J. Phys. Chem. Solids 129 (2019) 317-323.
19. G.S. Jamila, S. Sajjad, S.A.K. Leghari, T. Mahmood, Role of nitrogen doped carbon quantum dots on CuO nano-leaves as solar induced photo catalyst, J. Phys. Chem. Solids 138 (2020) 109233.
20. H. Chen, S.M. Park, J.H. Lee, X. Meng, D.W. Shin, J.B. Yoo, Large scale fabrication of single-crystal CuO nanoplatelets using a template-free hydrothermal approach, Electron. Mater. Lett. 4 (2008) 161-165.
21. L. Palliyaguru, U.S. Kulathunga, L.I. Jayarathna, C.D. Jayaweera, P.M. Jayaweera, A simple and novel synthetic route to prepare anatase TiO_2 nanopowders from natural ilmenite via the H_3PO_4/NH_3 process, Int. J. Miner. Metall. Mater. 27 (2020) 846-855.
22. S. Kumar, Influence of synthesis strategy on the formation of microspheres of self-assembled CuO rectangular nanorods and hierarchical structures of self-assembled Cu_2O nanospheres from single precursor (copper (II) acetate monohydrate) and their structural, optical, thermal and magnetic properties, Mater. Chem. Phys. 258 (2021) 123929.
23. L. Sinatra, A.P. LaGrow, W. Peng, A.R. Kirmani, A. Amassian, H. Idriss, O.M. Bakr, A Au/Cu_2O-TiO_2 system for photo-catalytic hydrogen production. A pn-junction effect or a simple case of in situ reduction?, J. Catal. 322 (2015) 109-117.
24. G. Yang, D. Gao, J. Zhang, J. Zhang, Z. Shi, D. Xue, Evidence of vacancy-induced room temperature ferromagnetism in amorphous and crystalline Al_2O_3 nanoparticles, J. Phys. Chem. C 115 (2011) 16814-16818.
25. F. Zuo, L. Wang, T. Wu, Z. Zhang, D. Borchardt, P. Feng, Self-doped Ti^{3+} enhanced photocatalyst for hydrogen production under visible light, J. Am. Chem. Soc. 132 (2010) 11856-11857.
26. Y. Liu, B. Zhang, L. Luo, X. Chen, Z. Wang, E. Wu, D. Su, W. Huang, TiO_2/Cu_2O core/ultrathin shell nanorods as efficient and stable photocatalysts for water reduction, Angew. Chem. 127 (2015) 15475-15480.

27. P.G. Harrison, I.K. Ball, W. Azelee, W. Daniell, D. Goldfarb, Nature and surface redox properties of copper (II)-promoted cerium (IV) oxide CO-oxidation catalysts, Chem. Mater. 12 (2000) 3715-3725.
28. T. Dhandayuthapani, R. Sivakumar, R. Ilangovan, Growth of micro flower rutile TiO_2 films by chemical bath deposition technique: Study on the properties of structural, surface morphological, vibrational, optical and compositional, Surf. Interfaces 4 (2016) 59-68.
29. G. Nabi, W. Raza, M.B. Tahir, Green synthesis of TiO_2 nanoparticle using cinnamon powder extract and the study of optical properties, J. Inorg. Organomet. Polym. Mater. 30 (2020) 1425-1429.
30. V. Kumaravel, S. Rhatigan, S. Mathew, M.C. Michel, J. Bartlett, M. Nolan, S.C. Pillai, Mo doped TiO_2: impact on oxygen vacancies, anatase phase stability and photocatalytic activity, J. Phys. Materials 3 (2020) 025008.
31. Q. Hua, T. Cao, H. Bao, Z. Jiang, W. Huang, Crystal-Plane-Controlled Surface Chemistry and Catalytic Performance of Surfactant-Free Cu_2O Nanocrystals, ChemSusChem 6 (2013) 1966-1972.
32. B. Bharti, S. Kumar, H.N. Lee, R. Kumar, R. Formation of oxygen vacancies and Ti^{3+} state in TiO_2 thin film and enhanced optical properties by air plasma treatment, Sci. Rep. 6 (2016) 32355.
33. C. Yu, D. Cai, K. Yang, C.Y. Jimmy, Y. Zhou, C. Fan, Sol–gel derived S, I-codoped mesoporous TiO_2 photocatalyst with high visible-light photocatalytic activity, J. Phys. Chem. Solids 71 (2010) 1337-1343.
34. F. Peng, L. Cai, L. Huang, H. Yu, H. Wang, Preparation of nitrogen-doped titanium dioxide with visible-light photocatalytic activity using a facile hydrothermal method, J. Phys. Chem. Solids 69 (2008) 1657-1664.
35. X. Yu, X. Fan, L. An, Z. Li, J. Liu, Facile synthesis of Ti^{3+}-TiO_2 mesocrystals for efficient visible-light photocatalysis, J. Phys. Chem. Solids 119 (2018) 94-99.
36. X. Zhang, L. Wang, C. Liu, Y. Ding, S. Zhang, Y. Zeng, Y. Liu, S. Luo, A bamboo-inspired hierarchical nanoarchitecture of Ag/CuO/TiO_2 nanotube array for highly photocatalytic degradation of 2, 4-dinitrophenol, J. Hazard. Mater. 313 (2016) 244-252.
37. G. Wang, Z. Fu, T. Wang, W. Lei, P. Sun, Y. Sui, B. Zou, A rational design of

hollow nanocages Ag@CuO-TiO_2 for enhanced acetone sensing performance, Sens. Actuators B Chem. 295 (2019) 70-78.

38. Y. Wang, Y. Lü, W. Zhan, Z. Xie, Q. Kuang, L. Zheng, Synthesis of porous Cu_2O/CuO cages using Cu-based metal–organic frameworks as templates and their gas-sensing properties, J. Mater. Chem. A 3 (2015) 12796-12803.
39. D.A. Svintsitskiy, T.Y. Kardash, O.A. Stonkus, E.M. Slavinskaya, A.I. Stadnichenko, S.V. Koscheev, A.P. Chupakhin, A.I. Boronin, In situ XRD, XPS, TEM, and TPR study of highly active in CO oxidation CuO nanopowders, J. Phys. Chem. C 117 (2013) 14588-14599.
40. Ç. Oruç, A. Altındal, Structural and dielectric properties of CuO nanoparticles, Ceram. Int. 43 (2017) 10708-10714.
41. D.A. Svintsitskiy, T.Y. Kardash, A.I. Boronin, Surface dynamics of mixed silver-copper oxide $AgCuO_2$ during X-ray photoelectron spectroscopy study, Appl. Surf. Sci. 463 (2019) 300-309.
42. A. Ganguly, S. Sharma, P. Papakonstantinou, J. Hamilton, Probing the thermal deoxygenation of graphene oxide using high-resolution in situ X-ray-based spectroscopies, J. Phys. Chem. C, 115 (2011) 17009-17019.
43. J. Yuan, J. Zhang, M.P. Yang, W.J. Meng, H. Wang, J.X. Lu, CuO nanoparticles supported on TiO_2 with high efficiency for CO_2 electrochemical reduction to ethanol, Catalysts 8 (2018) 171.
44. R. Yang, L. Yang, T. Tao, F. Ma, M. Xu, Z. Zhang, Contrastive study of structure and photocatalytic performance with three-dimensionally ordered macroporous CuO-TiO_2 and CuO/TiO_2, Appl. Surf. Sci. 288 (2014) 363-368.
45. Q. Zhang, L. Huang, S. Kang, C. Yin, Z. Ma, L. Cui, Y. Wang, CuO/Cu_2O nanowire arrays grafted by reduced graphene oxide: synthesis, characterization, and application in photocatalytic reduction of CO_2, RSC Adv. 7 (2017) 43642-43647.
46. D.A. Svintsitskiy, A.I. Stadnichenko, D.V. Demidov, S.V. Koscheev, A.I. Boronin, Investigation of oxygen states and reactivities on a nanostructured cupric oxide surface, Appl. Surf. Sci. 257 (2011) 8542-8549.
47. A.A. Ogwu, T.H. Darma, A reactive magnetron sputtering route for attaining a controlled core-rim phase partitioning in Cu_2O/CuO thin films with resistive switching potential, J. Appl. Phys. 113 (2013) 183522.

48. I.H. Chowdhury, S. Ghosh, S. Basak, M.K. Naskar, Mesoporous CuO-TiO_2 microspheres for efficient catalytic oxidation of CO and photodegradation of methylene blue, J. Phys. Chem. Solids 104 (2017) 103-110.
49. X.H. Xia, Y. Gao, Z. Wang, Z.J. Jia, Structure and photocatalytic properties of copper-doped rutile TiO_2 prepared by a low-temperature process, J. Phys. Chem. Solids 69 (2008) 2888-2893.
50. L.I. Ibarra-Rodríguez, A.M. Huerta-Flores, L.M. Torres-Martínez, Development of $Na_2Ti_6O_{13}$/CuO/Cu_2O heterostructures for solar photocatalytic production of low-carbon fuels, Mater. Res. Bull. 122 (2020) 110679.
51. C. Shifu, Z. Sujuan, L. Wei, Z. Wei, Study on the photocatalytic activity of p–n junction photocatalyst Cu_2O/TiO_2, J. Nanosci. Nanotechnol. 9 (2009) 4397-4403.
52. X. You, F. Chen, J. Zhang, M. Anpo, A novel deposition precipitation method for preparation of Ag-loaded titanium dioxide, Catal. Lett. 102 (2005) 247-250.
53. H. Zhang, C. Liang, J. Liu, Z. Tian, G. Wang, W. Cai, Defect-mediated formation of Ag cluster-doped TiO_2 nanoparticles for efficient photodegradation of pentachlorophenol, Langmuir 28 (2012) 3938-3944.
54. S.K. Pandey, M.K. Tripathi, V. Ramanathan, P.K. Mishra, D. Tiwary, Highly facile Ag/NiO nanocomposite synthesized by sol-gel method for mineralization of rhodamine B, J. Phys. Chem. Solids 159 (2021) 110287.
55. C. Ling, C. Yue, R. Yuan, J. Qiu, F.Q. Liu, J.J. Zhu, Enhanced removal of sulfamethoxazole by a novel composite of TiO_2 nanocrystals in situ wrapped-Bi_2O_4 microrods under simulated solar irradiation, Chem. Eng. J 384 (2020) 123278.
56. R. Zhou, S. Yang, E. Tao, L. Liu, J. Qian, The defect is perfect: MoS_2/TiO_2 modified with unsaturated Mo vacancies to construct Z-scheme heterojunction & improve mobility of e, J. Clean. Prod. 337 (2022) 130511.
57. K. Ding, D. Yu, W. Wang, P. Gao, B. Liu, Fabrication of multiple hierarchical heterojunction Ag@AgBr/$BiPO_4$/r-GO with enhanced visible-light-driven photocatalytic activities towards dye degradation, Appl. Surf. Sci. 445 (2018) 39-49.
58. M. Gao, L. Zhu, C.K. Peh, G.W. Ho, Solar absorber material and system designs for photothermal water vaporization towards clean water and energy production, Energy Environ. Sci. 12 (2019) 841-864.

59. G. Li, K.H. Wong, X. Zhang, C. Hu, C.Y. Jimmy, R.C.Y. Chan, P.K. Wong, Degradation of acid orange 7 using magnetic AgBr under visible light: the roles of oxidizing species, Chemosphere 76 (2009) 1185-1191.
60. B.J. Wiley, S.H. Im, Z.Y. Li, J. McLellan, A. Siekkinen, Y. Xia, Maneuvering the surface plasmon resonance of silver nanostructures through shape-controlled synthesis, J. Phys. Chem. B 110 (2006) 15666-15675.
61. Y. Duan, M. Zhang, L. Wang, F. Wang, L. Yang, X. Li, C. Wang. Plasmonic Ag-TiO_{2-x} nanocomposites for the photocatalytic removal of NO under visible light with high selectivity: The role of oxygen vacancies, Appl. Catal. B: Environ. 204 (2017) 67-77.
62. M. Janczarek, E. Kowalska, On the origin of enhanced photocatalytic activity of copper-modified titania in the oxidative reaction systems, Catalysts 7 (2017) 317.
63. P.L. Khoo, K. Satou, M. Izaki, The Electronic States of Copper Oxides Photoactive Layers Prepared by Electrodeposition Followed by Annealing, IOP Conf. Ser.: Mater. Sci. Eng. 920 (2020) 012028.
64. P. Basnet, E. Anderson, Y. Zhao, Hybrid Cu_xO–TiO_2 Nanopowders Prepared by Ball Milling for Solar Energy Conversion and Visible-Light-Induced Wastewater Treatment, ACS Appl. Nano Mater. 2 (2019) 2446-2455.
65. S. Banerjee, S.C. Pillai, P. Falaras, K.E. O'shea, J.A. Byrne, D.D. Dionysiou, New insights into the mechanism of visible light photocatalysis, J. Phys. Chem. Lett. 5 (2014) 2543-2554.
66. J. Hasan, H. Li, G. Tian, C. Qin, Fabrication of Cr_2S_3-GO-TiO_2 composite with high visible-light-driven photocatalytic activity on degradation of organic dyes, Chem. Phys. 539 (2020) 110950.